



FERMI GBM OBSERVATIONS OF LIGO GRAVITATIONAL-WAVE EVENT GW150914

V. CONNAUGHTON¹, E. BURNS², A. GOLDSTEIN^{3,20}, L. BLACKBURN^{4,5}, M. S. BRIGGS^{6,7}, B.-B. ZHANG^{7,8}, J. CAMP⁹, N. CHRISTENSEN¹⁰, C. M. HUI³, P. JENKE⁷, T. LITTENBERG¹, J. E. MCENERY⁹, J. RACUSIN⁹, P. SHAWHAN¹¹, L. SINGER^{9,20}, J. VEITCH¹², C. A. WILSON-HODGE³, P. N. BHAT⁷, E. BISSALDI^{13,14}, W. CLEVELAND¹, G. FITZPATRICK⁷, M. M. GILES¹⁵, M. H. GIBBY¹⁵, A. VON KIENLIN¹⁶, R. M. KIPPEN¹⁷, S. MCBREEN¹⁸, B. MAILYAN⁷, C. A. MEEGAN⁷, W. S. PACIESAS¹, R. D. PREECE⁶, O. J. ROBERTS¹⁸, L. SPARKE¹⁹, M. STANBRO⁶, K. TOELGE¹⁴, AND P. VERES⁷

¹Universities Space Research Association, 320 Sparkman Drive, Huntsville, AL 35806, USA; valerie@nasa.gov

²Physics Department, University of Alabama in Huntsville, 320 Sparkman Drive, Huntsville, AL 35805, USA

³Astrophysics Office, ZP12, NASA/Marshall Space Flight Center, Huntsville, AL 35812, USA

⁴Harvard-Smithsonian Center for Astrophysics, 60 Garden Street, Cambridge, MA 02138, USA

⁵LIGO, Massachusetts Institute of Technology, Cambridge, MA 02139, USA

⁶Department of Space Science, University of Alabama in Huntsville, 320 Sparkman Drive, Huntsville, AL 35805, USA

⁷CSPAR, University of Alabama in Huntsville, 320 Sparkman Drive, Huntsville, AL 35805, USA

⁸Instituto de Astrofísica de Andalucía (IAA-CSIC), P.O. Box 03004, E-18080 Granada, Spain

⁹NASA Goddard Space Flight Center, Greenbelt, MD 20771, USA

¹⁰Physics and Astronomy, Carleton College, MN 55057, USA

¹¹Department of Physics, University of Maryland, College Park, MD 20742, USA

¹²University of Birmingham, Birmingham B15 2TT, UK

¹³Istituto Nazionale di Fisica Nucleare, Sezione di Bari, I-70126 Bari, Italy

¹⁴Dipartimento di Fisica, Politecnico di Bari, I-70125, Bari, Italy

¹⁵Jacobs Technology, Inc., Huntsville, AL, USA

¹⁶Max-Planck-Institut für extraterrestrische Physik, Giessenbachstrasse 1, D-85748 Garching, Germany

¹⁷Los Alamos National Laboratory, NM 87545, USA

¹⁸School of Physics, University College Dublin, Belfield, Stillorgan Road, Dublin 4, Ireland

¹⁹NASA Headquarters, Washington DC, USA

Received 2016 March 1; revised 2016 May 22; accepted 2016 May 27; published 2016 July 13

ABSTRACT

With an instantaneous view of 70% of the sky, the *Fermi* Gamma-ray Burst Monitor (GBM) is an excellent partner in the search for electromagnetic counterparts to gravitational-wave (GW) events. GBM observations at the time of the Laser Interferometer Gravitational-wave Observatory (LIGO) event GW150914 reveal the presence of a weak transient above 50 keV, 0.4 s after the GW event, with a false-alarm probability of 0.0022 (2.9σ). This weak transient lasting 1 s was not detected by any other instrument and does not appear to be connected with other previously known astrophysical, solar, terrestrial, or magnetospheric activity. Its localization is ill-constrained but consistent with the direction of GW150914. The duration and spectrum of the transient event are consistent with a weak short gamma-ray burst (GRB) arriving at a large angle to the direction in which *Fermi* was pointing where the GBM detector response is not optimal. If the GBM transient is associated with GW150914, then this electromagnetic signal from a stellar mass black hole binary merger is unexpected. We calculate a luminosity in hard X-ray emission between 1 keV and 10 MeV of $1.8_{-1.0}^{+1.5} \times 10^{49}$ erg s⁻¹. Future joint observations of GW events by LIGO/Virgo and *Fermi* GBM could reveal whether the weak transient reported here is a plausible counterpart to GW150914 or a chance coincidence, and will further probe the connection between compact binary mergers and short GRBs.

Key words: gamma-ray burst: general – gravitational waves

1. INTRODUCTION

The Gamma-ray Burst Monitor (GBM) on the *Fermi* Gamma-ray Space Telescope is an all-sky, hard X-ray monitor that is ideally suited to detect rare and unpredictable transient events. Since the launch of *Fermi* in 2008 June, GBM has triggered on board nearly 5000 times in response to short-lived impulsive bursts of photons lasting from under a millisecond to hundreds of seconds. This collection of triggered events²¹ includes nearly 1800 gamma-ray bursts (GRBs; von Kienlin et al. 2014), 1100 solar flares, 200 bursts from 9 separate magnetars, and over 600 terrestrial gamma-ray flashes (TGFs). Dedicated offline searches over all or parts of the mission have yielded over 200 additional magnetar bursts (Collazzi

et al. 2015), thousands of additional TGFs²² (Briggs et al. 2013), nearly 700 type I thermonuclear bursts from galactic binary systems (Jenke et al. 2016), non-impulsive steady or variable emission from over 100 mostly galactic sources (Wilson-Hodge et al. 2012)²³, and pulsed emission from 35 accretion-powered galactic binary systems.²⁴

Detection of gravitational waves (GW) reported by the Laser Interferometer Gravitational-wave Observatory (LIGO; LIGO Scientific Collaboration et al. 2015) and the Virgo experiment (Acernese et al. 2015) has been eagerly anticipated. LIGO and Virgo are sensitive to the GW produced by the mergers of stellar mass compact objects in a binary system as well as other sources. The most promising electromagnetic counterpart to a

²⁰ NASA Postdoctoral Fellow.

²¹ <http://heasarc.gsfc.nasa.gov/W3Browse/fermi/fermigtrig.html>

²² <http://fermi.gsfc.nasa.gov/ssc/data/access/gbm/taf/>

²³ <http://heastro.phys.lsu.edu/gbm/>

²⁴ <http://gamma-ray.nsstc.nasa.gov/gbm/science/pulsars.html>

compact binary merger involving a neutron star is a short GRB. Berger (2014) provides a recent review of short GRBs and Fong et al. (2015) summarize what has been learned from observing their afterglows. The joint GW-GRB detection rate is expected to be low given the collimation of the GRB emission (both prompt and afterglow radiation) and the detection horizons of LIGO and Virgo for these progenitors (Siellez et al. 2014). Other electromagnetic counterparts have been suggested, notably optical/infrared transients from the decay of r-process isotopes produced in the ejecta resulting from the binary merger, kilonovae, also known as macronovae (Li & Paczyński 1998; Metzger et al. 2010; Barnes & Kasen 2013; Tanaka & Hotokezaka 2013). Only one such event has been reported (Berger et al. 2013; Tanvir et al. 2013) with another candidate identified for a short burst with extended emission (Yang et al. 2015). Owing to their intrinsic faintness, kilonovae are detected only nearby, an observational constraint aggravated by the need for short GRB localizations accurate enough to enable deep observations of the kilonova signal. Unlike GRBs and their afterglow, however, kilonovae are expected to be isotropic, so that mergers observed off-axis by LIGO can still be probed for such a signature. GBM has detected 300 short GRBs since the launch of *Fermi*, a rate of ~ 40 per year (von Kienlin et al. 2014). An offline search of the GBM data yields an additional 35 short GRB candidates per year, most of them unverified by other instruments. Validating these additional short GRB candidates and refining the search criteria will allow the GBM team to deploy an efficient pipeline for the identification and communication in near real-time of sub-threshold short GRBs during upcoming observing runs of the LIGO and Virgo experiments.

Independently of this offline untargeted search of the GBM data, we developed a targeted search and efficient data analysis pipelines to identify in the GBM data the electromagnetic counterparts to any candidate GW events. We exercised and refined these pipelines during Advanced LIGO’s summer 2015 engineering runs in preparation for the first Advanced LIGO observing run (O1). The search procedures and parameters, which we present here, were established a priori so that when LIGO began operations, we could find candidate counterparts automatically and establish their significance. Joint localization of these events may improve the localizations done separately, which could assist follow-up observers with pointed instruments in identifying the host galaxy and thus the redshift of the source. On 2015 September 16, the LIGO and Virgo collaborations reported that a candidate event, G184098, had been identified in data recorded on September 14 (The LIGO Scientific Collaboration & Virgo 2015d; Abbott et al. 2016b).²⁵ The candidate was subsequently characterized as being consistent with a signal from the merger of a stellar mass black hole binary system (The LIGO Scientific Collaboration & Virgo 2015a) with a false-alarm rate (FAR) of less than one per century (The LIGO Scientific Collaboration & Virgo 2015c), and was announced publicly in Abbott et al. (2016b) as GW event GW150914. Although there are no predictions or well-established mechanisms for detectable EM emission from stellar mass binary black hole mergers to guide a search for

counterparts in the GBM data, we carried out a methodical search around the time and sky location of the event GW150914, which we report in the following section.

2. GBM OBSERVATIONS OF GW150914

GBM consists of 12 Thallium-doped Sodium Iodide (NaI) detectors with a diameter of 12.7 cm and a thickness of 1.27 cm and two Bismuth Germanate (BGO) detectors with a diameter and thickness of 12.7 cm (Meegan et al. 2009). The NaI detectors are sensitive between 8 keV and 1 MeV and the BGO detectors extend the energy range to 40 MeV. The GBM flight software was designed so that GBM can trigger on board in response to impulsive events if the count rates recorded in two or more NaI detectors significantly exceed the background count rate on at least one timescale (from 16 ms to 4.096 s) in at least one of three energy ranges above 50 keV (50–300 keV, >100 keV, >300 keV). Strong background variations below 50 keV hinder the simple background fitting needed for automated operation on the spacecraft. On short timescales, the variations are less significant and triggering can be enabled in the 25–50 keV range on timescales below 128 ms, resulting in the on board detection of 200 magnetar bursts. GBM data can be probed at longer timescales and lower energy ranges in offline searches dedicated to particular objects, including type I thermonuclear bursts (Jenke et al. 2016) and additional, weaker magnetar bursts (Collazzi et al. 2015). The modification of the GBM flight software to include data from the BGO detectors in the 16 ms triggering window has made GBM very sensitive to spectrally harder events associated with the electric fields in thunderstorms, TGFs (Briggs et al. 2013).

GBM has an instantaneous sky coverage of about 70%, with the remainder blocked by the Earth. GBM operates continuously, except when detector high voltages are turned off during passages of the *Fermi* spacecraft through regions of high particle precipitation activity in the South Atlantic Anomaly (SAA), $\sim 15\%$ of the time depending on where *Fermi* is in the ~ 50 day precession cycle of its orbit. GBM was recording data (i.e., not in the SAA) continuously from nearly 2 hr before to over 7 hr after the GW event. Figure 1 shows the LIGO sky map from Abbott et al. (2016b) with the shaded region indicating the region of sky occulted to *Fermi* by the Earth at the time of detection of the GW event. GBM observed 75% of the probability region in the location map during the detection of GW150914, with the full region becoming visible 25 minutes later.

GBM did not record any on board triggers around the time of the GW detection, at 09:50:45.391 UT on 2015 September 14. The triggers closest in time were from two events on 2015 September 14 that are consistent with particle precipitation in or near the spacecraft, at 04:09:23 UT on entering the SAA and at 14:21:34 UT when *Fermi* was at high geomagnetic latitude, nearly 6 hr before and 4.5 hr after the GW event, respectively. GBM recorded triggers at similar points in the *Fermi* orbit on the preceding and following days, leaving no doubt as to their magnetospheric origin. These two triggered events were sufficiently far removed in time from GW150914 to ensure that GBM was operating in a nominal configuration in which it could have triggered on significant transient sources above the on board threshold.

²⁵ Information about GW event candidates and follow-up observations was exchanged in Gamma-ray Coordinates Network (GCN) Notices and Circulars which initially were restricted to groups which had established agreements with LIGO and Virgo. The Circulars regarding G184098 were added to the public archive when the details of GW150914 were published.

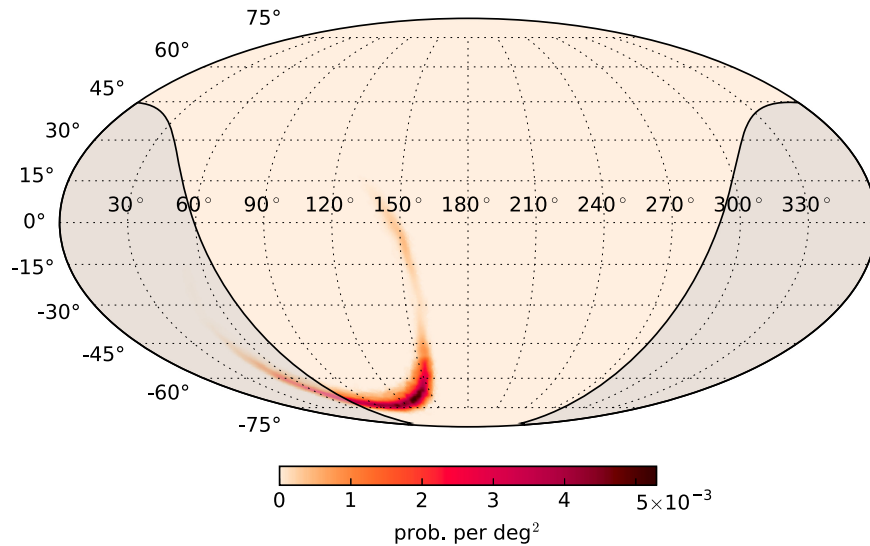


Figure 1. Localization map for GW150914, the GW event reported in Abbott et al. (2016b). The gray shaded region indicates the region of sky occulted to *Fermi* by the Earth at the time of GW150914. The region not occulted by the Earth contains 75% of the probability of the localization map, with all but 6% of the probability contained in the southern portion of the annulus. The entire region was visible to *Fermi* GBM 25 minutes after the GW event was detected.

2.1. Detection and Significance of the Weak, Hard X-Ray Event GW150914-GBM

An offline search of the GBM Continuous Time-tagged Event (CTTE) data for impulsive events too weak to trigger on board *Fermi*, or from a sky position unfavorable to the two-detector on board triggering requirement, was implemented in 2015. The main motivation for this offline search is to increase the sensitivity of GBM to short GRBs during the period in which *Fermi*, LIGO, and Virgo operate jointly. The offline search currently operates on CTTE data from the 12 NaI detectors over four energy bands (27–540, 50–540, 100–540, and 100–980 keV) and 10 timescales from 0.1 to 2.8 s. The detection threshold for each search algorithm is set so that the joint chance probability of the signals in any detector combination exceeding background levels above the lowest threshold level is 10^{-6} in one day. We estimate that this improves GBM sensitivity to short GRBs by a factor of 2–3 in burst count fluence and the offline search detection rate of 1–4 candidate short GRBs per month is consistent with this estimate. The offline search reports no candidates above the detection threshold on the day of the GW event.²⁶

In addition to this undirected offline search, a targeted search of the GBM data was developed during S6, i.e., the last observing run of the previous configuration of LIGO (Blackburn et al. 2015a). By searching both the GW and GBM data sets, the significance of a sub-threshold signal in one can be strengthened by the detection of a signal in the other, provided that the false positive rate of the joint search is characterized and the detection levels in both instruments are selected accordingly. It is estimated that the horizon of LIGO/Virgo can be boosted by 15%–20% through this validation of sub-threshold candidates (Kochanek & Piran 1993; Kelley et al. 2013; Blackburn et al. 2015a). The directed search of the GBM data is seeded with the time and (optionally) the sky location of any LIGO/Virgo candidate event. A coherent search over all GBM detectors (NaI and BGO) using the full instrument response at each sky position is performed over a user-specified time

window, assuming one of three template source spectra, revealing short-duration candidates typically between 0.256 to 8 s in duration, as described in Appendix A. The candidates are ranked by a Bayesian likelihood statistic.

The model spectra for each tested source location are Band functions with three sets of parameters spanning the range of astrophysical phenomena we expect to uncover. Emission from galactic transients, solar flares, and soft GRBs is expected to favor a soft spectrum. Long GRBs are typically best fit with a moderate spectrum, and a hard spectrum is often preferred for short GRBs. The values for the parameters of the Band function (Band et al. 1993), two power-law indices and a peak energy, are those used in the standard GBM source localization process (Connaughton et al. 2015): $\alpha, \beta, E_{\text{peak}} = (-1.9, -3.7, 70 \text{ keV})$, $(-1, -2.3, 230 \text{ keV})$, and $(0, -1.5, 1 \text{ MeV})$, for the soft, moderate, and hard spectra, respectively. The response to each spectrum is evaluated over all sky locations with an option to use a known source position as a prior in the evaluation of the likelihood. Events, characterized by their time and duration, are ranked by their likelihood ratios after marginalizing over their unknown source amplitude, spectrum, and sky position. We note that these spectral models are used as templates to identify candidates in the data, allowing a sky-position-dependent deconvolution of our data to evaluate the significance of any candidate across all detectors. No optimization of the models or of their parameters is performed. Because a trial factor is required for each template, we use only three models spanning a large parameter space from very soft to very hard, without any preconception about which type of event we are seeking. Spectral analysis of any candidate is performed at a later stage (Section 3.2).

We searched 30 s of GBM data before and after the LIGO coalescence time for a plausible counterpart with duration between 0.256 and 8 s. The $\pm 30 \text{ s}$ interval we use was selected a priori and is roughly guided by observation: if GRBs are related to compact binary mergers, then we expect the impulsive gamma-ray emission to be close in time to the GW, suggesting an interval of just a few seconds for our search. Precursors to short GRBs have, however, been observed earlier than $\sim 10 \text{ s}$ prior to the main emission (Koshut

²⁶ http://gamma-ray.nsstc.nasa.gov/gbm/science/sgrb_search.html

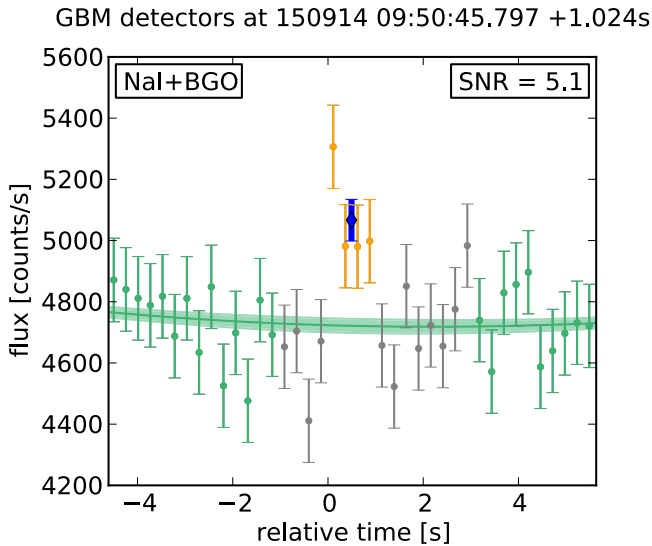


Figure 2. Model-dependent count rates detected as a function of time relative to the start of GW150914-GBM, ~ 0.4 s after the GW event. The raw count rates are weighted and summed to maximize the signal to noise for a modeled source. CTIME time bins are 0.256 s wide. The green data points are used in the background fit. The gold points are the counts in the time period that shows significant emission, the gray points are outside this time period, and the blue point shows the 1.024 s average over the gold points. For a single spectrum and sky location, detector counts for each energy channel are weighted according to the modeled rate and inverse noise variance due to background. The weighted counts from all NaI and BGO detectors are then summed to obtain a signal-to-noise optimized light curve for that model. Each model is also assigned a likelihood by the targeted search based on the foreground counts (in the region of time spanned by the gold points), and this is used to marginalize the light curve over the unknown source location and spectrum.

et al. 1995; Burlon et al. 2009; Troja et al. 2010), and may originate from a less collimated emission region that is observable even when the GRB jet is not along the line of sight to the detector.

An all-sky search of the GBM data revealed two candidates below a threshold of 10^{-4} Hz chance probability. One transient, occurring at 09:50:56.8 (11 s after GW150914), was visible only below 50 keV, favored the soft model spectrum, and lasted 2 s. Using the standard GBM localization procedure, we found a source position of R.A., decl. = $267^{\circ}.7$, $-22^{\circ}.4$ with a 68% statistical uncertainty region of radius 15° and a systematic error of around 3° , as described in Connaughton et al. (2015). At a position in Galactic coordinates of $l, b = 6^{\circ}.2$, $2^{\circ}.4$, the event is compatible with an origin near the galactic center, well separated from and incompatible with the LIGO localization region. It is typical of the type of soft X-ray transient activity seen regularly in the GBM background data, particularly from the galactic center region. We do not view this transient event as being possibly related to GW150914 and we will not discuss it further.

The search also identified a hard transient which began at 09:50:45.8, about 0.4 s after the reported LIGO burst trigger time of 09:50:45.4, and lasted for about 1 s. The temporal offset of 0.4 s is much longer than the light travel time of 2–45 ms between *Fermi* and the LIGO detectors. The detector counts best matched those predicted from a hard model spectrum. We reported this event in Blackburn et al. (2015b); henceforth, we call it GW150914-GBM. Figure 2 shows the model-dependent light curve of GW150914-GBM, where the detector data have been summed using weights that maximize the signal to noise

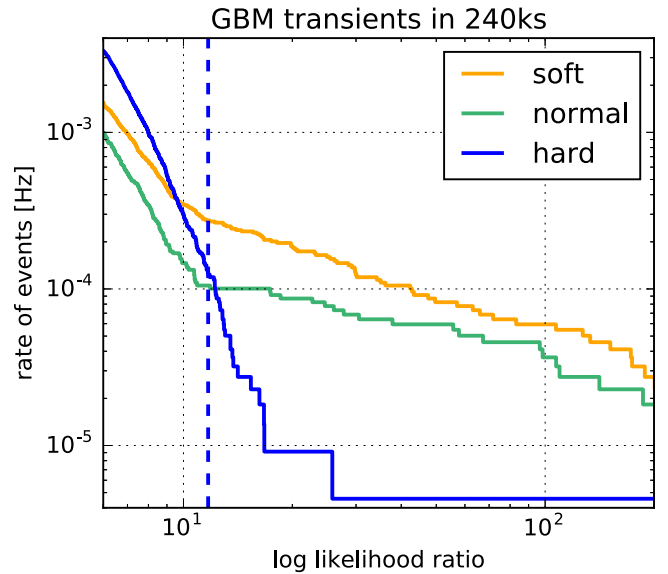


Figure 3. Distribution of transients identified by the targeted search pipeline in ± 120 ks of GBM data surrounding GW150914. The events are between 0.256 and 8.192 s in duration and sorted by best-fit spectral type. The dotted blue line marks the likelihood ratio assigned to nearby candidate GW150914-GBM, while the long-tail in the blue curve (hard spectrum) represents the single on board triggered GRB in the data sample. The green and gold curves show the candidates that favor the other template spectra used in the search.

for a given source model, and the unknown source model itself is weighted according to its likelihood in the data.

2.2. The Rate of Detection of Short Hard Transients in the GBM Data

The association of a likelihood value with a FAR is based on an analysis of two months of GBM data from 2009–2010 (Blackburn et al. 2015a). The FAR for GW150914-GBM, 10^{-4} Hz, is very close to the reporting threshold for the search. The likelihood value for GW150914-GBM is much lower than those obtained for two weak short GRBs detected by *Swift* that did not cause an on board GBM trigger but were found in a targeted search, and much higher than three weak short GRBs that were undistinguishable above the background in the GBM data using our targeted search (Blackburn et al. 2015a). Because the likelihood value was so close to our reporting threshold, we considered the possibility that the background count rates might be higher in 2015 than when the search criteria and FAR were evaluated, implying a higher FAR than 10^{-4} Hz for GW150914-GBM. We used our targeted search to examine 240 ks of GBM data from 2015 September with 218822.1 s of GBM livetime, excluding passages of *Fermi* through or close to the SAA where the detectors are turned off or count rate increases overwhelm any attempt to fit a reasonable background model. We find 27 events above our threshold, for a FAR of 1.2×10^{-4} Hz, in agreement with the previously estimated value. The distribution of events found in the 240 ks interval is shown in Figure 3. This gives a 90% upper limit on the expected background of hard transients of 35 in this much livetime, or 1.60×10^{-4} Hz.

We determine the significance of a GBM counterpart candidate by considering both its frequency of occurrence and its proximity to the GW trigger time. Our method, described in Blackburn (2015) and attached as Appendix B to this work, allows us to account for all of the search windows in

the interval over which we performed our search, while assigning larger significance to those events found closest to the time of interest. This two-parameter ranking method frees us from having to choose a fixed search interval, and we can also limit the length of the search interval to a value that is computationally reasonable.

With a FAR of 1.60×10^{-4} Hz for GW150914-GBM, which begins 0.4 s after the time of the GW event, we calculate using Equation (8) a post-trial false-alarm probability for GW150914-GBM, $P = 2 \times 3 \times 1.60 \times 10^{-4} \text{ Hz} \times 0.4 \text{ s} \times (1 + \ln(30 \text{ s}/0.256 \text{ s})) = 0.0022$ (2.9σ), where the logarithmic term accounts for the trial factor from multiple coincidence windows and the factor of 2 accounts for the search window on either side of the GW time. A trial factor of 3 is included to account for the three spectral templates, which were treated as independent owing to their very different distributions.

Our motivation for incorporating the temporal offset from the GW event into our likelihood ranking statistic is that we have a prior expectation that inspirals occur almost simultaneously with GRB production. We do have a motivation for a search window that is long compared to the typical short GRB duration of 2 s so that our search is sensitive to precursors up to a few tens of seconds before the GW event. Most short GRBs do not, however, show precursor activity, and so our a priori assumption is that a nearly simultaneous GBM transient is more likely to be associated with the GW event than one that is 10 s beforehand. The false-alarm probability of coincidence scales very slowly with the selection of our window. For example, if ± 60 s were used instead, then our calculated false-alarm probability would increase by only 12%. Thus, we believe that our ranking strategy helps to reduce the dependence of calculated significance on specific tuning of these search parameters. If we assume, instead, a uniform probability across the 60 s window, then we obtain a post-trial false-alarm probability of $1 - \exp(-60 \times 3 \times 1.60 \times 10^{-4}) = 0.028$ (1.9σ).

We now explore in detail whether the GBM data for GW150914-GBM suggest an astrophysical origin and, if so, whether the source is consistent with GW150914 or can be attributed to other causes. We note that nothing in the following sections changes the FAR or the FAP that we present above. If further analysis of the data for GW150914-GBM suggested a non-physical source spectrum, or if the inferred brightness of the event proved incompatible with upper limits set by complementary observations, then this would lend support to a non-astrophysical nature for the event, but it would not change the FAR of the event or increase the probability that it occurred so close to GW150914 by chance. Similarly, if the search technique we developed proved inefficient, we could in principle improve our ability to discern real events and reject false ones, obtaining a lower FAR for a source associated with a given likelihood value. While we do not rule out future improvements based on our experience during O1, we do not attempt here to improve our search a posteriori.

3. CHARACTERISTICS OF GW150914-GBM

Each GBM detector provides a different observational perspective. The relative rates in the NaI detectors establish the arrival direction of a source. From the distribution of counts as a function of energy, we infer something about its nature. In Appendix C, we show that the detector pattern of GW150914-GBM is unusual, with all of the individual detector count rates

being slightly above background, simultaneously. We also show that the count spectrum from the NaI detectors (summed) is consistent with the count spectrum from the BGO detectors (summed), indicating a reasonable physical spectrum that peaks in the BGO energy range.

3.1. Localization

The angular response of the NaI detectors allows the reconstruction of the most likely arrival direction of an impulsive event, based on the differences in background-subtracted count rates recorded in 12 NaI detectors that have different sky orientations. A bright source is localized with a 68% confidence level statistical error of minimum 1° set by the resolution of a reference grid, and a systematic error that we have characterized in Connaughton et al. (2015) as about 3° – 4° . We can localize GW150914-GBM only roughly, as described in Appendix D, to a region covering 3000 square degrees (68% confidence level), with a most likely location of R.A., decl. = 75° , -73° . The source direction is underneath the spacecraft, at an angle of 163° to the spacecraft pointing direction, with 52% of the probability region above the Earth limb and the rest hidden by the Earth.

GBM was not designed to detect sources under the spacecraft, that have large angular offsets, θ , to the spacecraft pointing direction. The pre-launch plan for *Fermi* nominal operations was to observe at a 30° angle from the local zenith, allowing the sky to drift across the field of view, rocking the spacecraft north and south on alternate ~ 90 minute spacecraft orbits to achieve even sky coverage for the Large Area Telescope (LAT) survey of the high-energy sky. The GBM detectors were placed for maximum sensitivity to sources in the LAT field of view ($\theta = 0$ – $\sim 65^\circ$), with good sensitivity out to $\theta < \sim 120^\circ$. The Earth was expected to block the high θ regions, which are, by design, not well-viewed by the NaI detectors. The sky survey mode was changed after launch to alleviate the effect of higher-than-expected battery temperatures on the mission lifetime. A 50° rocking profile was found to keep the batteries cooler and is now the nominal sky survey mode, with the result that GBM has more exposure to sky regions at high θ angles than expected when deciding the detector placement. The combination of the declining sensitivity of the NaI detectors at large angles to the detector normals and the two-detector on board trigger requirement results in very few GRBs being detected with arrival directions at very high θ .

Of the 1776 GRBs listed in the Browse Table at the HEASARC²⁷, only 67 occur at a θ larger than 130° , and only 3 larger than 160° , with none of the latter category being short GRBs. One of the GRBs detected beyond 160° , GRB130306A, was also detected by *Swift*. Because of the large uncertainty region associated with GW150914-GBM, it is difficult to assess exactly how close its arrival direction is to that of GRB130306A, but NaI 5 has the smallest angle to the source direction in both cases, and NaI 9 the largest. GRB130306A showed roughly equal signals in all NaI detectors, except NaI 10 and NaI 11, which were fainter. GRB130306A was a bright GRB with a localization by GBM that was less than 2° from the *Swift* localization and a statistical uncertainty of 1° . This indicates that GBM is capable of localizing an event from an arrival direction beneath the spacecraft, from which nearly

²⁷ <http://heasarc.gsfc.nasa.gov/W3Browse/fermi/fermigtrig.html>

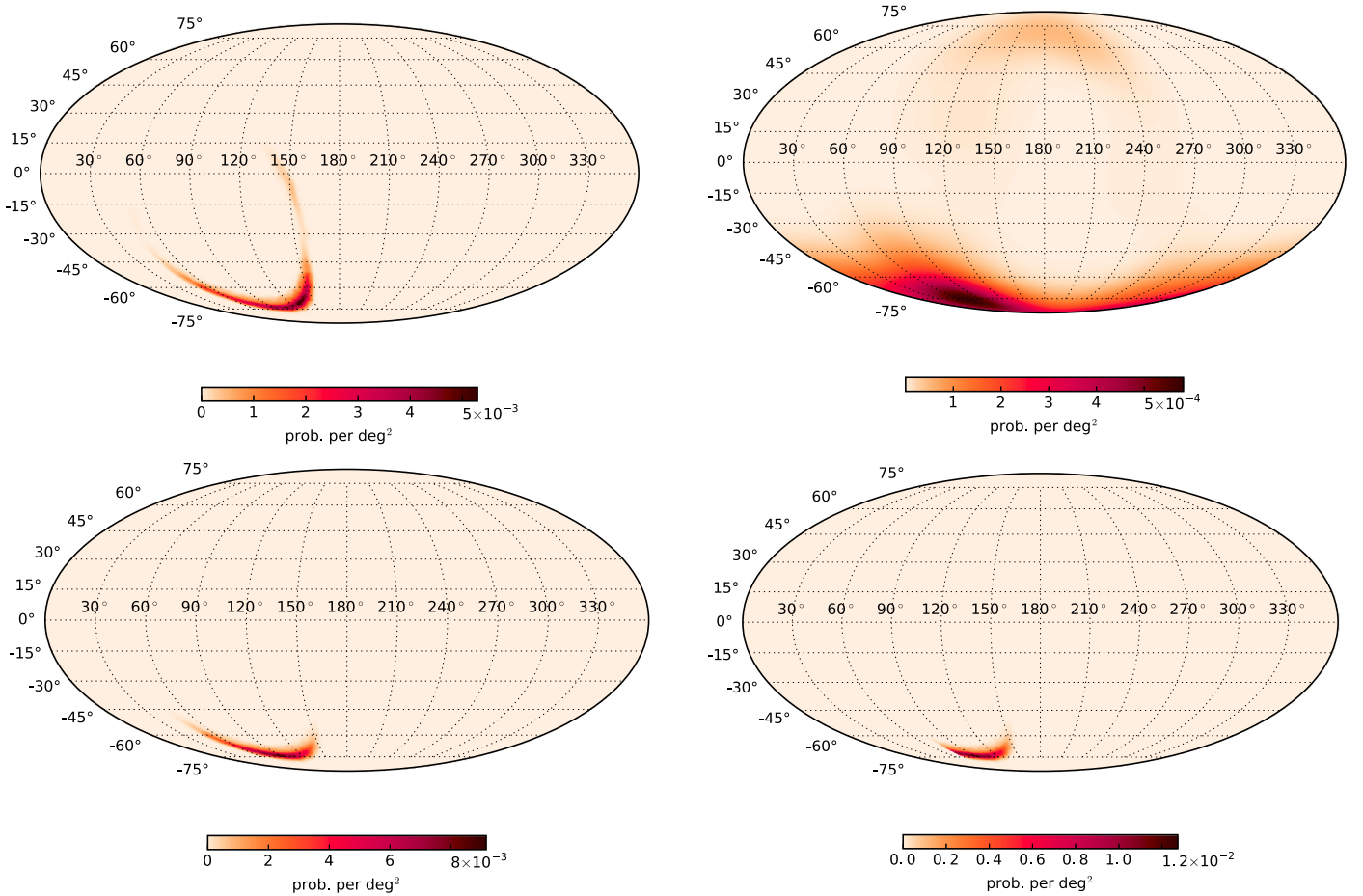


Figure 4. The LIGO localization map (top left) can be combined with the GBM localization map for GW150914-GBM (top right) assuming GW150914-GBM is associated with GW150914. The combined map is shown (bottom left) with the sky region that is occulted to *Fermi* removed in the bottom right plot. The constraint from *Fermi* shrinks the 90% confidence region for the LIGO localization from 601 to 199 square degrees.

equal count rates are expected in most of the NaI detectors if the event is bright enough.

We find that the localization of GW150914-GBM is consistent with part of the LIGO localization annulus. If the transient event uncovered in the GBM data is associated with GW150914, then the GBM probability map can be combined with the LIGO annulus to shrink the 90% confidence level LIGO localization by 2/3, as shown in Figure 4.

3.2. Energy Spectrum of GW150914-GBM

The data for GW150914-GBM imply a weak but significant hard X-ray source with a spectrum that extends into the MeV range and a location that is consistent with an arrival direction along the southern lobe of the sky map for GW150914. Converting the observed counts in the GBM detectors to a source flux requires a deconvolution of the instrumental response with an assumed spectral model. We sample a range of arrival directions along the observed LIGO location arc, using the data and associated responses for the detectors at each location that are most favorably oriented to the arrival direction. Table 2 suggests that NaI 5 and BGO 0 are the most suitable detector set for all of the locations along the arc. We use the *rmfit* spectral fitting package²⁸, which takes a forward folding approach to determine the parameters that best fit the

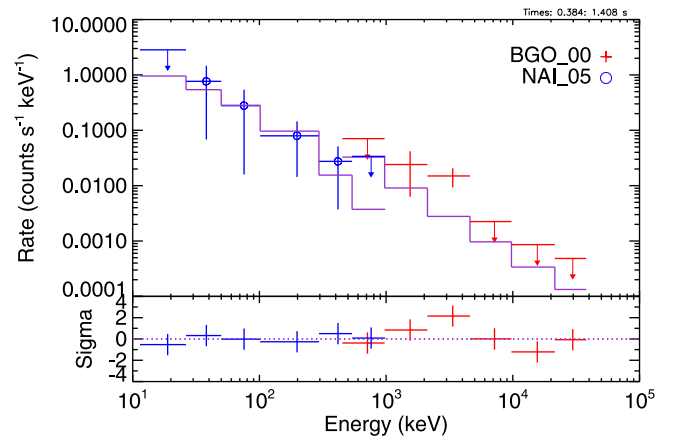


Figure 5. Power-law fit to the data from 0.384 to 1.408 s relative to the time of GW150914, from NaI 5 (blue) and BGO 0 (red), corresponding to the high time bin in Figure 7. The symbols show the data. The solid line shows the best-fit power-law model. Residuals on the bottom panel show scatter but no systematic deviation. We cannot use the first and last energy channels in either detector data type (there are threshold effects and electronic overflow events), leaving the data from 12 energy channels included in the fit.

data for any model, given the instrumental response. The minimization routine producing the best-fit parameters uses a likelihood-based fitting statistic, CSTAT.

Because the event is very weak, we do not attempt to fit the full-resolution data (128 energy channels). Instead, we bin the

²⁸ <http://fermi.gsfc.nasa.gov/ssc/data/analysis/rmfit/>

CTTE data into the eight native CTIME energy bins, and use the CTIME energy responses in our fits. In principle, binning in energy is unnecessary because a likelihood-based statistic correctly accounts for low count rates in individual energy channels. In practice, the implementation of CSTAT in our spectral fitting software neglects background fluctuations as a separate contribution to the uncertainty in the total count rates in the GBM data, an effect that is mitigated by rebinning the data prior to fitting. A consequence of this limitation of CSTAT is that the uncertainties on the parameters returned by the fits are almost certainly underestimated. In the analysis that follows, we report 68% statistical uncertainties, with the caveat that the true uncertainties are probably higher. GRB spectra are well represented by empirical functions with power-law components around a peak energy in the spectral energy distribution, E_{peak} . The Band function is used when there are enough counts to constrain all parameters, particularly the high-energy power-law index, β . If β is not constrained, a power-law fit with an exponential cut-off above E_{peak} , called the Comptonized model, generally works well. For the weakest bursts, or when E_{peak} lies outside the energy range of the instrument, a power-law fit is adequate and serves to provide an estimate of the flux and fluence of the burst as long as the energy range over which the flux and fluence are calculated is not extended outside the observation range. We find that for all 11 positions along the LIGO arc, a power-law fit to the data from GW150914-GBM can be constrained. For one of the positions, we can also provide weak constraints for a fit to the Comptonized model. Figure 5 shows a representative count spectrum and power-law model fit to the data from 0.384 to 1.408 s relative to the time of GW150914, with a deconvolution assuming the source lies near the central position of the southern arc. For each of the 11 positions along the arc, we find the best-fit power-law index and associated amplitude. We use these parameters to simulate each spectrum 10^4 times, using the resulting distribution to estimate the uncertainties on the parameter values (68% confidence level). We also sample the parameter distributions to calculate the fluence and its confidence region, weighting the sampling along the arc according to the LIGO localization probability contained near each point on the arc. We obtain a best-fit power-law index $-1.40_{-0.24}^{+0.18}$ and amplitude $0.002_{-0.001}^{+0.002}$ photons $\text{s}^{-1} \text{cm}^{-2} \text{keV}^{-1}$ over the LIGO localization arc, yielding a fluence between 10 and 1000 keV of $2.4_{-1.0}^{+1.7} \times 10^{-7} \text{erg cm}^{-2}$.

For a deconvolution assuming a source position at the northeastern tip of the southern lobe (entry 10 in Table 2), the Comptonized model converges to find a best-fit E_{peak} of $3.5_{-1.1}^{+2.3}$ MeV with a power-law index below E_{peak} of $-0.16_{-0.50}^{+0.57}$, although this fit is not statistically preferred over the power-law fit. When simulating iterations of the burst to obtain 68% confidence level uncertainties on the parameters, the fit failed about 50% of the time. The fluence between 10 and 1000 keV obtained assuming a Comptonized model for a source from this position is $2.8_{-0.9}^{+1.0} \times 10^{-7} \text{erg cm}^{-2}$.

The fit parameter values are typical for short GRBs, with power-law indices of about -1.4 found in cases where the GRB is too weak to constrain E_{peak} , and values for the Comptonized fit parameters that are not unusual for short GRBs (Gruber et al. 2014). A fluence of $2.4 \times 10^{-7} \text{erg cm}^{-2}$ is nearly average for short GRBs, with 40% of short GRBs detected by GBM weaker than this value.²⁹ The least energetic

short GRBs detected by GBM have a fluence an order of magnitude smaller than GW150914-GBM, implying that if GW150914-GBM is a short GRB, then with a more favorable arrival direction, it would have caused an on board trigger. If GW150914-GBM is part of the short GRB population, then its fluence is not atypical but its unfortunate arrival direction yields only a weak signal in GBM. Figure 5 shows that the model is a reasonable fit to the count spectrum even at low energies, implying no paucity of counts at low energies in NaI 5, which is the only detector with a small enough viewing angle to the source position to have any sensitivity below 50 keV.

At a distance of 410_{-180}^{+160} Mpc implied by the GW observations (Abbott et al. 2016b), we obtain a source luminosity of $1.8_{-1.0}^{+1.5} \times 10^{49} \text{erg s}^{-1}$ in the 1 keV–10 MeV energy range that is standard for reporting such bolometric luminosities. The uncertainties reflect the range of possible distances to the progenitor, uncertainties in the spectral fit parameters (using the power-law fits), and the range of arrival directions along the arc. This luminosity is an order of magnitude dimmer than the peak luminosities of the dimmest short GRBs in the sample analyzed by Wanderman & Piran (2015).

3.3. Other Observations of GW150914-GBM

Instruments other than GBM can also detect impulsive events in the hard X-ray energy range. No pointed instruments reported observations of GW150914, suggesting that they were not looking in that direction at the time of the GW event.

Upper limits to the emission from GW150914 from the non-detection by instruments on board the Astrorivelatore Gamma a Immagini Leggero (AGILE) close in time to the GW event are reported by Tavani et al. (2016). The MicroCalorimeter had non-optimal exposure to the GW event, from which upper limits to GW150914-GBM are calculated that are compatible with the GBM fluence. The other instruments on board AGILE observed most of the LIGO annulus hundreds of seconds on either side of the GW event, but not at the time of the event.

The anti-coincidence shield (ACS) of the Spectrometer on board INTEGRAL (SPI) has a large collection area above 80 keV with an all-sky response that is not hindered by Earth occultation (von Kienlin et al. 2003). We looked for a signal in SPI-ACS at the time of GW150914-GBM and found no excess above background.³⁰ The SPI-ACS team reported a fluence limit of $1.3 \times 10^{-7} \text{erg cm}^{-2}$ in the 100 keV–100 MeV energy range based on a null detection over a 1 s period (Ferrigno et al. 2015). Further analysis of the SPI-ACS data is reported in Savchenko et al. (2016). They estimate a source signal between 5 and 15σ above background should have been seen in the SPI-ACS data if the source were represented by the Comptonized spectrum found in a fit to the GBM data assuming one position on the LIGO arc but applied to source positions along the LIGO arc. We note that this spectrum was fit to the GBM data (but not statistically favored) only for a source position that is excluded by the GBM localization and is thus not reliable. A power law in energy with an index of about -1.4 was the only fit we could constrain for a source at any position on the LIGO arc. Because power-law fits without a break are generally not physical representations of a source spectrum, a fluence calculation for the expected response in a detector with a different energy-dependent response than the instrument in

²⁹ <http://heasarc.gsfc.nasa.gov/W3Browse/fermi/fermigbrst.html>

³⁰ <http://isdc.unige.ch/~savchenk/spiacs-online/spiacs-ipnlc.pl>

which the power-law fit was measured is not realistic. Instead, Savchenko et al. (2016) calculate the expected SPI-ACS signal assuming various spectral shapes in an extrapolation from the central value for the fluence obtained in fits to the GBM data. They report 3σ fluence limits that are compatible with the 3σ fluence extrapolations obtained in fits to the GBM data using the same assumed models.

von Kienlin et al. (2003) and Savchenko et al. (2016) report that the sensitivity of SPI-ACS is a strong function of the source energy spectrum and, to a lesser extent, the exposure of the detectors to the source location. In principle, non-detection by SPI-ACS can be used to further constrain the spectrum and arrival direction of GW150914-GBM, or indeed any event. If there is no allowed spectrum and location that can accommodate both an interpretation of the GBM excess as real and the non-detection by the SPI-ACS, then we would conclude that a GBM signal was not astrophysical. In the case of GW150914-GBM, the non-detection would appear to rule out a source with a spectrum fit to the data using a Comptonized model assuming a source position that is not compatible with the GBM/LIGO localization, but not with the spectrum that was actually obtained in a fit to the data assuming source positions compatible with the joint GBM/LIGO localization. In practice, there are large uncertainties in both the spectrum and arrival direction of the source, and we need a systematic study of the GBM and SPI-ACS sensitivities. The SPI-ACS data are recorded with no energy resolution, as the sum of nearly 100 detectors with different orientations, so that a joint fit to GBM and SPI-ACS data is really a prediction of the total counts expected in the SPI-ACS data given a spectral fit obtained using the GBM data alone. In the case of GW150914-GBM, the GBM data alone cannot rule out a spectrum as hard as the model template in the discovery pipeline—the event is too weak to characterize the signal beyond a simple power-law fit and the BGO collection area above 10 MeV is too small for a detectable signal in an event this weak. In principle, with an understanding of systematic uncertainties in both the GBM fits and the cross-calibration of the two instruments, the flat response of the SPI-ACS above 10 MeV could constrain the spectral shape of GW150914-GBM.

Further investigation of the SPI-ACS detection sensitivity to GBM-detected GRBs as a function of the GRB spectrum is ongoing, in order to evaluate the relative sensitivities of the two instruments to short GRBs, a study involving both instrument teams that will include systematic effects that are neglected both here and in Savchenko et al. (2016).

3.4. Possible Origins for GW150914-GBM

The energy spectrum of GW150914-GBM is too hard for any of the galactic transient sources detected by GBM (bursts from magnetars, type I thermonuclear X-ray bursts, or outbursts from accreting pulsars) and also too hard to be of solar origin. Additionally, the Sun was quiet around the time of the GW event detection. The localization (Appendix D) close to the Earth's limb raises the question of whether GW150914-GBM comes from the Earth.

TGFs emit gamma-rays extending to at least 40 MeV. TGFs are detected either as gamma-rays produced by electrons accelerated in electric fields in thunderstorms, or as secondary electrons and positrons guided by the magnetic field line that connects a thunderstorm to a gamma-ray detector. Typical durations for the gamma-ray and electron events are several

hundred μ s and several to tens of ms, respectively, much shorter than GW150914-GBM (Briggs et al. 2013). TGF gamma-rays are detected by GBM when the source is within 800 km of the *Fermi* nadir; the charged particle form can be detected from thousands of kilometers from the source, but only when GBM is within the \sim 100 km diameter beam centered on the magnetic field line from the source (Dwyer et al. 2008; Briggs et al. 2011, 2013). The World Wide Lightning Network (WWLLN; Rodger et al. 2009; Hutchins et al. 2012), a global network of VLF radio receivers, virtually always finds clusters of lightning (i.e., thunderstorms) for GBM TGFs. At the time of GW150914-GBM, WWLLN has no lightning detections over \pm 10 minutes within 800 km of the spacecraft nadir or at the two magnetic footprints, making it very unlikely that there were TGF sources within GBM's detection range.

Another lightning detection network, GLD360 (Said et al. 2010, 2013), reported a very high peak current lightning stroke at 09:50:45.406 at latitude $11^{\circ}.1685$, longitude $-3^{\circ}.2855$. At more than 4000 km from *Fermi*, this is past the horizon so that gamma-rays would be blocked by the Earth. The magnetic field line from this source passes thousands of kilometers to the west of *Fermi*, so if any charged particles were emitted, they would not be transported to *Fermi*.

At the time of the GW event, *Fermi* was at low geomagnetic latitude and was not near the SAA. While we cannot exclude a magnetospheric origin for GW150914-GBM, the observing conditions were not conducive to such an event, nor is the light curve typical of magnetospheric activity, which is usually manifested as longer and smoother (tens of seconds) bumps above background.

3.5. Search for Steady Emission from Known or Unknown Sources Near the LIGO Localization Region

Using various search techniques, we found (i) no evidence for long-term steady emission from the direction of GW150914-GBM, (ii) no evidence for contamination by known sources of hard X-ray emission of any search for emission related to GW150914-GBM, and (iii) no evidence for non-impulsive emission related to the GW event in the days surrounding the event.

In addition to GBM's role as a powerful detector of transient, impulsive sources, the Earth occultation technique (EOT) allows GBM to perform as an all-sky monitor of sources emitting hard X rays at levels typically undetectable above the GBM background. This technique involves modeling the GBM background count rates when a potential source of hard X rays sets or rises from behind the Earth. Candidate sources are monitored³¹ with around 100 having been significantly detected to date above 10 mCrab between 12 and 25 keV (Wilson-Hodge et al. 2012). Of the 246 sources that are monitored, 5 lie within 5° of the LIGO localization region for GW150914: LMC X-2, the flat spectrum radio quasar PKS 0601-70, the gamma-ray binary system 2FGL J 1019.0-5856, and the accreting X-ray binary pulsars GRO J1008-57 and RX J0520.5-6932 (which were detected in hard X-ray emission by *Swift* Burst Alert Telescope in 2013³²). Only GRO J1008-57 has previously been detected by GBM through the EOT. Both of the accreting pulsars lie within 3° of the LIGO error region

³¹ <http://heastro.phys.lsu.edu/gbm/>

³² <http://swift.gsfc.nasa.gov/results/transients/>

and have been detected in the past through the GBM pulsar monitoring program, which is more sensitive to pulsed emission than the EOT is to non-pulsed emission. We looked for pulsed emission from these accreting pulsars on 2015 September 14 and find that they are not currently active. We also used a blind frequency search for pulsed emission from 24 positions along the Galactic plane and from the direction of the Small and Large Magellanic Clouds. We did not detect any signal within or near the LIGO localization region. In any search for long-lived emission in the days around the detection of the GW event, we do not, therefore, expect contamination from known sources of hard X-ray emission above the GBM EOT and accreting pulsar detection thresholds.

The daily sensitivity of the EOT is about 100 mCrab. The EOT can resolve signals from sources 2° apart. We divided the full LIGO arc into 34 resolvable positions (all but one along the southern lobe of the arc) and looked for mission-long activity from these positions, as well as daily emission around the time of the GW event. We examined three years of data using the EOT, from 2013 January 1 through 2016 January 29. Long-term averages were consistent with no detections for the 12–25, 25–50, 50–100, 100–300, and 300–500 keV energy bands. We also looked for emission on a daily timescale for the month of September 2015 without detecting any of the sources during the month surrounding the LIGO GW event time.

The EOT fails to measure source fluxes if the angle between the tangent to the Earth's limb and the spacecraft orbit normal, β , exceeds 66.5° . At grazing incidence, the Earth occultation transition becomes too extended in time (>20 s from 100%–0% atmospheric transmission), and at β values beyond grazing incidence, the source is not occulted by the Earth at all. This occurs at certain points in the ~ 50 day *Fermi* orbital precession cycle for high declination sources ($>\pm 40^\circ$) owing to the relative geometry of the source position and the *Fermi* orbital inclination of 26.5° . Only 13 of the targets, with right ascensions from 48° – 77° , and the northern lobe position, had usable Earth occultation measurements spanning the time of the LIGO event. The remaining targets with right ascensions from 74° – 155° had no usable Earth occultation measurements from before the time of the LIGO event until two or more days after GW150914. Another way to look at this is that these unocculted positions never set behind the Earth and were observed by GBM with 85% exposure, losing only the time that *Fermi* crossed through the SAA. For much of the LIGO arc during the days around the GW event detection, GBM was thus exceptionally sensitive to any impulsive emission that would have triggered the instrument.

If GW150914-GBM is related to the GW event, and the localization is in the region of the LIGO arc with $\beta \sim 66.5^\circ$, i.e., very close to being occulted by the Earth, then grazing Earth occultations could be responsible for a reduction of flux below 50 keV through atmospheric absorption (Figure 6) and could potentially be used to further improve the source location. Lower energy photons, e.g., 12–25 keV, can be fully blocked (0% atmospheric transmission) before the 100–300 keV band reaches 50% transmission. We cannot exclude the possibility that the spectral analysis (and thus the luminosity estimate) is affected by partial, energy-dependent atmospheric absorption of the signal, but the spectral deconvolution of the data from NaI 5 (Section 3.2) does not suggest a deficit of counts below 50 keV relative to the model. It is more likely that the source is not close to being occulted by

the Earth and, instead, that the hard spectrum observed in most of the detectors is a mixture of intrinsic spectral hardness and the large viewing angles to most of NaI detectors which lead to preferential detection of higher-energy photons and absorption of photons of lower energy in the instrument material behind the scintillator.

The LIGO localization arc for GW150914 became observable by the *Fermi* LAT ~ 4000 s after the GW event and a search for high-energy emission over timescales comparable to our search in hard X rays with the EOT is reported by Fermi-LAT Collaboration (2016). A summary of observations of GW150914 is given in Abbott et al. (2016a).

4. DISCUSSION AND OUTLOOK FOR JOINT LIGO-GBM SCIENCE

GBM observed over 75% of the probability in the GW event sky location at the time of GW150914. A weak hard X-ray transient lasting around 1 s was detected above 50 keV 0.4 s after the GW event using a technique developed to find short transients in the GBM data in coincidence with sub-threshold GW events. The chance probability of finding such an event within the time interval we searched is 0.2% following the assumption, made a priori, that the likelihood of a counterpart associated with the GW event is higher for an event closer to the time of the GW event, and 2.8% if we assume equal probability of association across the 60 s search window. The GBM signal is localized to a region consistent with the LIGO sky map with a large uncertainty on the location. If the transient event uncovered in the GBM data is associated with GW150914, then it is possible that its origin under the *Fermi* spacecraft, combined with the weakness of the source, can account for the lack of confidence associated with the standard localization procedure applied to this event. If we assume that the LIGO and GBM events have a common origin, then combining the LIGO and GBM localization maps reduces the LIGO localization area by 2/3.

The transient event cannot be attributed to other known astrophysical, solar, terrestrial, or magnetospheric activity. The distribution of detected counts as a function of energy appears reasonable among detectors across the energy range 50 keV–4.8 MeV. Spectral deconvolution yields a fluence (68% confidence level) over the 1 s duration of $2.4_{-1.0}^{+1.7} \times 10^{-7}$ erg cm $^{-2}$ between 10 keV and 1 MeV, comparable to moderate intensity short GRBs on which GBM has triggered. This implies that with a more favorable arrival geometry, this event could have triggered GBM on board at the time of the GW detection, providing a real-time localization within seconds of the trigger. A real-time electromagnetic counterpart to a GW event informs follow-up observers that an afterglow signal may be detectable along the line of sight, and the GBM location helps in reducing the number of observations needed to cover the LIGO localization region.

The collection area of SPI-ACS is a factor of ~ 30 – 40 times greater than that of a GBM BGO detector, but the upper limits imposed by the non-detection of GW150914-GBM by SPI-ACS are close to the fluence values calculated for the GBM transient, despite the unfavorable source direction for GBM and the optimum source direction for SPI-ACS. Because of uncertainties in the energy spectrum and location of GW150914-GBM, and because of instrumental and background systematic effects on the calculation of the fluence of GW150914-GBM, any tension between the GBM and

INTEGRAL SPI-ACS observations will likely be resolved only with future joint observations of GW events.

The detection of an electromagnetic counterpart to a merger of stellar mass black holes would be a surprising event. Kamble & Kaplan (2013) explore possible weak signatures to such mergers, with uncertainties surrounding the formation of circumbinary disks and associated magnetic fields. Although circumbinary disks are expected to form around supermassive black holes (Mayer et al. 2007), there is no such prediction for stellar mass systems. Moreover, the GBM signal appears similar to a short GRB, both in duration (less than 2 s), and in energy spectrum (peaked near an MeV). Models for short GRBs from compact binary progenitors always involve a neutron star, with short GRBs more easily produced from two neutron stars, unless the black hole companion has a high initial spin (Giacomazzo et al. 2013). A luminosity of $1.8_{-1.0}^{+1.5} \times 10^{49}$ erg s⁻¹ (between 1 keV and 10 MeV) for a short GRB, assuming the source distance of 410_{-180}^{+160} Mpc implied by the GW observations (Abbott et al. 2016b), is an order of magnitude dimmer than the peak luminosities of the dimmest short GRBs in the sample analyzed by Wanderman & Piran (2015). By another measure of brightness, the isotropic-equivalent energy release, also measured between 1 keV and 10 MeV, GW150914-GBM would also be dimmer than most short GRBs, but similar in magnitude to GRB050709 and GRB080905A, which were also nearby ($z = 0.161$ and 0.122 , respectively), and an order of magnitude dimmer in isotropic-equivalent energy release than the next dimmest short GRB reported in Giacomazzo et al. (2013) and D’Avanzo et al. (2014). If GW150914-GBM is a short GRB, then it was detected only because it was nearby. Based on the population of short GRBs with known redshifts, the contribution of such under-luminous events to the overall short GRB population detected by GBM is negligible, unless they form a separate class of nearby, sub-luminous events.

Our observation of GW150914-GBM has spurred investigations into complementary observations that may reveal afterglow signatures of such events (Morsony et al. 2016; Yamazaki et al. 2016), a possible mechanism to extract high-energy emission from stellar mass black hole mergers (Zhang 2016), unusual environments for the black hole merger that may lead to sufficient surrounding material to fuel the production of the GRB (Loeb 2016; Perna et al. 2016), implications of our observation if the association between GW150914 and GW150914-GBM is real (Ellis et al. 2016; Li et al. 2016), as well as arguments against the association being real, based on the difficulties of extracting enough energy from the black hole merger (Lyutikov 2016).

Further observations by LIGO and Virgo in coincidence with a detector sensitive to hard X-ray or gamma-ray transient events will determine whether short bursts of high-energy electromagnetic radiation accompany stellar mass black hole binary mergers. Because of the weakness of GW150914-GBM and its large localization uncertainty, chance coincidence may play a role in both the identification of GW150914-GBM as an astrophysical phenomenon and its association with the GW event, even with the false-alarm probability of 0.0022 that we calculate in Section 2.2. If the association is real, then the alignment of the merger axis with our line of sight may be attributed in part to the greater sensitivity of LIGO to on-axis events, but we would not expect most GW signals from BH

mergers to be accompanied by the detection of collimated electromagnetic transients. Another possibility is that the electromagnetic emission is not narrowly collimated and we can expect further joint detections of stellar mass black hole binary mergers and GRBs. This paradigm may be in tension with the non-detection of GW candidates in the last science runs of the previous configuration of LIGO/Virgo, S6/VSR2&3 (Abadie et al. 2012). None of the GRBs with known redshift detected during S6/VSR2&3 was within the BBH detection horizon (~ 100 Mpc). It is possible, however, that some of the 90% of GRBs with unknown redshifts were within the BBH horizon, which is, nonetheless, much closer than most short GRBs.

Analysis of the GBM data corresponding to all of the sub-threshold GW events from the O1 initial science operation period of LIGO is in progress. We have developed pipelines and data products to rapidly search the GBM data for counterparts to any GW events and communicate their localization to electromagnetic observers within hours of the GW event (depending on data downlink from the *Fermi* spacecraft).

Given the detection of GW150914 as a GW event from a stellar mass black hole binary system, then with all but the most pessimistic predictions, the detection of the weaker GW signals from neutron star binary systems is expected no later than 2019, when LIGO/Virgo reach full sensitivity. If this detection occurs during O2, the second observing run of LIGO and the initial deployment of Virgo, expected later in 2016, then our GBM-LIGO/Virgo pipelines are ready. Even if the association between GW150914-GBM and GW150914 is spurious, we expect to detect short GRBs from neutron star binary systems. With its broad field of view and good sensitivity at the peak emission energies for short GRBs, *Fermi* GBM is an ideal partner in the search for electromagnetic signals in coincidence with GW detections. Joint observations by *Fermi* and LIGO/Virgo will either confirm or exclude the connection between compact binary systems and short GRBs within a few years.

The authors acknowledge an ongoing collaborative effort and significant contributions to this paper from the LIGO/Virgo Consortium. They thank Marica Branchesi for her co-leadership of the LIGO/Virgo electromagnetic follow-up group, for providing prompt alerts and other information pertaining to the GW event. The GBM project is supported by NASA. Support for the German contribution to GBM was provided by the Bundesministerium für Bildung und Forschung (BMBF) via the Deutsches Zentrum für Luft und Raumfahrt (DLR) under contract number 50 QV 0301. A.v.K. was supported by the Bundesministeriums für Wirtschaft und Technologie (BMWi) through DLR grant 50 OG 1101. A.G. and L.S. are funded through the NASA Postdoctoral Fellowship Program. O.J.R. acknowledges support from Science Foundation Ireland under grant No. 12/IP/1288. J.V. was supported by STFC grant, ST/K005014/1. N.C. acknowledges NSF grant, PHY-1505373. The authors wish to thank the World Wide Lightning Location Network (<http://wwlln.net>), a collaboration among over 50 universities and institutions, for providing the lightning location data used in this paper. The authors are grateful to Sylvia Zhu for a critical reading of the manuscript and for her helpful suggestions.

APPENDIX A A TARGETED SEARCH OF GBM DATA

The targeted search attempts to identify short-duration (~ 1 s) excesses of counts recorded across the detectors that stand out over a smoothly varying background and that are consistent with a modeled point-source contribution from an astrophysical event. The seeding is done in time and sky position, where the seed time defines a limited (\sim minutes) period of time to scan and a seed sky-position prior can be used to inform the model prior.

The short-duration excess of counts from an astrophysical event are hypothesized to occur over a foreground interval $[t - T/2, t + T/2]$. Trial foreground durations T are spaced in powers of 2 between 0.256 and 8.192 s, and for a given duration, central times t are chosen at 75% time-interval overlap. This choice approximately preserves signal-to-noise mismatch across the search space. The technique was developed prior to the availability of CTTE data, using CTIME data, which are natively binned in 0.256 s accumulations with counts binned in eight energy channels. The counts registered in the 14 GBM detectors and 8 energy channels are evaluated independently for each detector-channel combination. For each short foreground interval $[t - T/2, t + T/2]$, we estimate the background rate at t using a polynomial fit to local data from $[t - 10T, t + 10T]$ (minimum ± 5 s), excluding time $[t - 3T/2, t + 5T/2]$ around the foreground interval to avoid bias from an on-source excess. The polynomial degree is determined by the interval length to account for more complicated background variability over longer intervals. It ranges from 2 (minimum) to $1 + 0.5 \log_2 T$.

A likelihood-ratio statistic is constructed for measured counts within this foreground interval that compares the hypothesis that detector counts arise from the expected background contribution plus a modeled signal (hypothesis H_1) to the hypothesis that observed counts arise from variations in estimated background rates alone (hypothesis H_0). The likelihood of observed background-subtracted counts $\tilde{d}_i = d_i - \langle n_i \rangle$ to have arisen solely from background fluctuations alone is

$$P(d_i|H_0) = \prod_i \frac{1}{\sqrt{2\pi}\sigma_{n_i}} \exp\left(-\frac{\tilde{d}_i^2}{2\sigma_{n_i}^2}\right), \quad (1)$$

where i runs over all independent measurements from detector-channel combinations (14 detectors, 8 channels) and σ_{n_i} represents the standard deviation for each measurement under a Gaussian approximation to the Poisson process. If we include expected source contributions $r_i s$ (source amplitude s subject to instrument response r_i) to each measurement from a modeled source, then the likelihood becomes

$$P(d_i|H_1) = \prod_i \frac{1}{\sqrt{2\pi}\sigma_{d_i}} \exp\left(-\frac{(\tilde{d}_i - r_i s)^2}{2\sigma_{d_i}^2}\right), \quad (2)$$

where a different standard deviation σ_{d_i} is used because the source contribution adds additional Poisson variation and systematic error. Assuming that Poisson and systematic errors can be approximated as Gaussian,

$$\sigma_{d_i}^2 = \sigma_{n_i}^2 + r_i s + \sigma_{r_i}^2 s^2 \quad (s \geq 0) \quad (3)$$

$$\sigma_{n_i}^2 = \langle n_i \rangle + \sigma_{b_i}^2, \quad (4)$$

where $\langle n_i \rangle$ is the estimated background, $\sigma_{r_i}^2$ represents systematic error in the model response, and $\sigma_{b_i}^2$ represents systematic error in the estimated background (e.g., fit uncertainty). The log-likelihood-ratio $\ln[P(d_i|H_1)/P(d_i|H_0)]$ captures the relative support in the data for hypothesis H_1 versus H_0 , and ranks plausible foreground windows in the GBM data.

Through the predicted counts $r_i s$, the likelihood ratio is dependent on assumed source amplitude at the Earth s , as well as source spectrum, position on the sky, and Earth position (during the foreground interval)—all of which influence the model response r_i . A semi-analytic approximate marginalization over source amplitude s is performed in log-likelihood space, using a power-law prior that favors directions in which the detector array is more sensitive. Marginalization over source location and spectrum is done numerically, after folding in any potential location prior. The maximum-likelihood spectrum is also recorded in order to further classify events. The use of a foreground interval has implicitly assumed a rectangular light curve prior with constant spectrum. Marginalization is not done over foreground interval, but instead a down-selected set of non-overlapping foreground windows with maximum likelihood are saved as event candidates. Further details are provided in Blackburn et al. (2015a).

APPENDIX B SIGNIFICANCE OF TWO-PARAMETER COINCIDENCE

Consider a background of Poisson-distributed events (Ross 2014) with a particular rate distribution in threshold parameter ρ , and thus the density and cumulative distributions are $d\lambda_c/d\rho_{\text{th}}$ and $\lambda_c(\rho_{\text{th}})$, where we have used subscripts on λ_c and ρ_{th} to emphasize the use of cumulative rate (rate of events with $\rho > \rho_{\text{th}}$). We would like to calculate the significance (accidental coincidence probability) of an event from this population falling within T of a time-of-interest t_0 . Ordinarily, one could pick in advance a single threshold ρ_{th} giving a single rate λ_c , then use the Poisson probability of falling within a certain time window $P(\Delta t < T) = 1 - e^{-\lambda_c T} \approx \lambda_c T$ for small P . If many different thresholds are tested, then the accidental coincidence probability may be multiplied by a trials factor representing the different effective populations of events.

It is convenient to not have to choose a particular threshold in advance, and thus be able to consider a wide range of possible event rates. In this case, one must generate a single detection statistic to rank plausible coincidences between events characterized by the two parameters ρ (or equivalently λ_c) and T (closeness to t_0). A natural ordering is by inverse false-alarm probability $R = (\lambda_c T)^{-1}$. $\lambda_c T$ was the original accidental coincidence probability P for a single threshold, but in this case we must add up contributions to accidental coincidence from all possible combinations of λ_c and T in order to get a faithful representation of the probability of a coincidence happening with greater R than our event under consideration. We can calculate the expected number of more highly ranked events:

$$N(R > 1/\lambda_c T) = \int_0^\infty d\lambda \int_0^{\lambda_c T/\lambda} dt e^{-t} d\lambda. \quad (5)$$

By representing the calculation as a sum over slivers of $d\lambda$, we can conveniently bypass details about the actual shape of $\lambda_c(\rho_{\text{th}})$. Each sliver actually has the same Poisson distribution

Table 1

 Signals in the GBM Detectors in σ Deviation from a Background fit for the 1.024 s High Bin in Figure 7

NaI 0	NaI 1	NaI 2	NaI 3	NaI 4	NaI 5
1.31	1.81	0.64	1.05	2.42	1.68
NaI 6	NaI 7	NaI 8	NaI 9	NaI 10	NaI 11
1.31	1.64	1.45	2.20	1.61	0.66
BGO 0	BGO 1				
2.25	2.56				

$d\lambda e^{-t d\lambda} = d\lambda + O(d\lambda^2)$ since they all cover the same amount of differential rate. However the order itself is determined by the cumulative rate, which sets the limit of integration. The exponential reduces to first order in infinitesimal $d\lambda$ (flat) and the integral becomes

$$N(R > 1/\lambda_c T) = \int_{\lambda_{\min}}^{\lambda_{\max}} d\lambda \frac{\lambda_c T}{\lambda} = \lambda_c T \ln\left(\frac{\lambda_{\max}}{\lambda_{\min}}\right). \quad (6)$$

Here, λ_{\max} and λ_{\min} are necessary for convergence.

λ_{\max} is naturally constrained by the production threshold of the events, or by the minimum measurable coincidence time $\lambda_{\max} T_{\min} = \lambda_c T$. We can also choose a maximum coincidence

window T_{\max} , up to the livetime of the experiment, to set $\lambda_{\min} T_{\max} = \lambda_c T$. Events from $0 < \lambda < \lambda_{\min}$ will still contribute to the accidental coincidence probability but subject to a bounded interval of time T_{\max} . Therefore, we need to add a constant to the expectation value equal to $\lambda_c T$. Under these constraints, the expected number becomes

$$N(R > 1/\lambda_c T) = \lambda_c T \left[1 + \ln\left(\frac{\lambda_{\max} T_{\max}}{\lambda_c T}\right) \right] \quad \text{or} \quad (7)$$

$$N(R > 1/\lambda_c T) = \lambda_c T \left[1 + \ln\left(\frac{T_{\max}}{T_{\min}}\right) \right] \quad (8)$$

depending on the choice of using λ_{\max} or T_{\min} . A two-sided coincidence window will multiply N by a trial factor of two. The accidental coincidence probability $P \approx N$ for small N .

APPENDIX C DETECTOR DATA FOR GW150914-GBM

Figure 6 shows the count rate registered in all 14 GBM detectors, with a zero time centered on the detection time of the GW event. In Figure 7, the counts are summed over all the detectors. The time binning of 1.024 s was one of six timescales (from 0.256 to 8.192 s in multiples of two) selected a priori

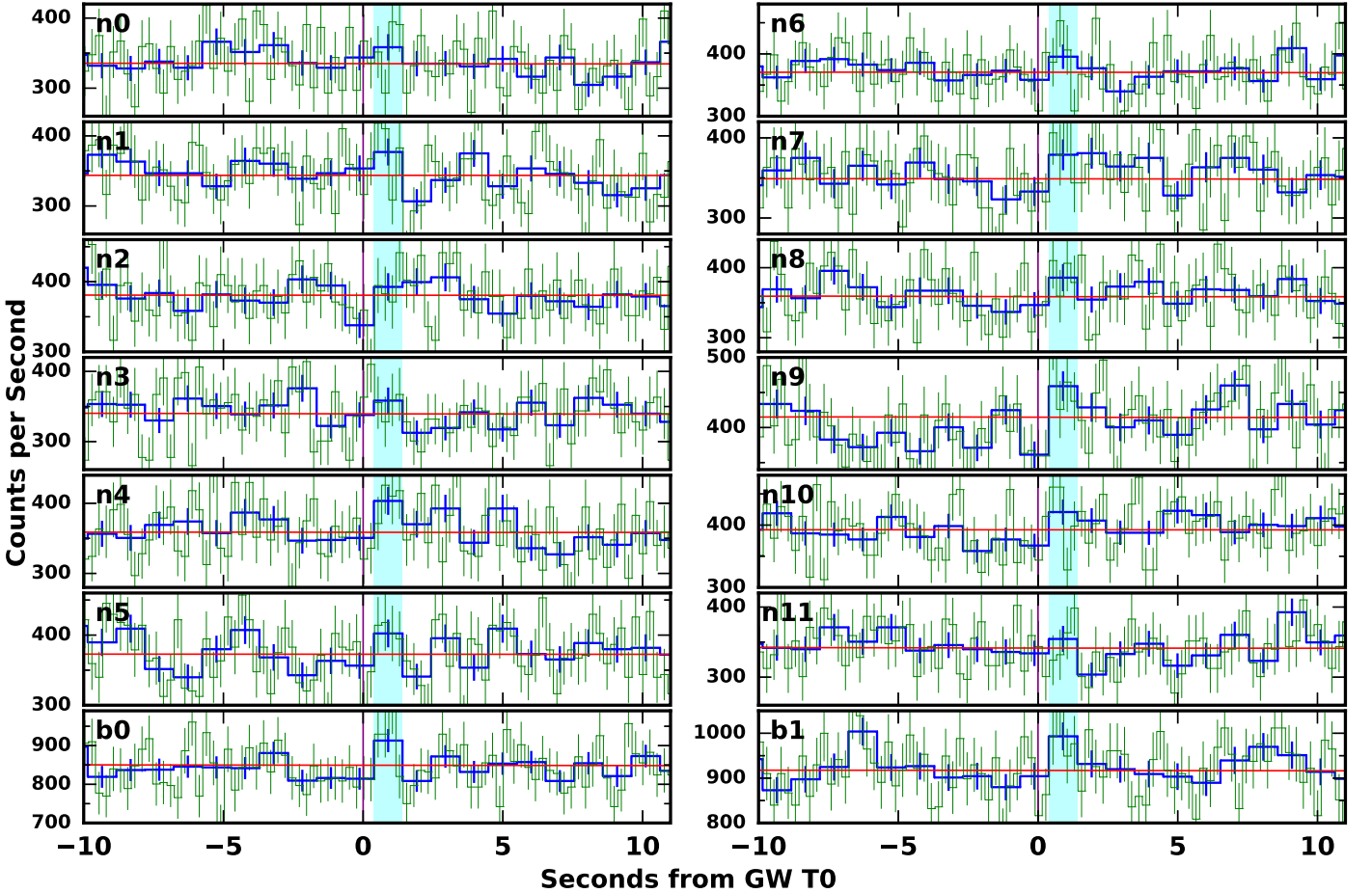


Figure 6. Count rates detected as a function of time relative to the detection time of GW150914 in each of the 14 GBM detectors. The shaded region is the time interval of GW150914-GBM, beginning 0.384 s after GW150914, at 09:30:45.775 UT. Time bins are 1.024 s wide and the red line indicates the background. The blue light curve was constructed from CTTE data, rebinned to optimize the signal-to-noise ratio. The 0.256 s CTIME binning is overplotted on the 1.024 s light curve. NaI data are summed over 50–980 keV and BGO data over 420 keV–4.7 MeV. The detector angles to different sky positions on the LIGO localization map are given in Table 2.

Table 2
Sky Locations on LIGO Localization Arc for GW150914 that Were Visible to GBM at the Time of the GW Event

R.A.	decl.	SC ϕ	SC θ	Nal 0	1	2	3	4	5	6	7	8	9	10	11	BGO 0	1	Prob. %
83.98	-72.85	342	160	144.8	122.0	83.1	117.8	76.1	71.2	161.5	142.0	97.3	149.2	103.3	108.6	70.8	109.2	12.1
101.99	-73.87	349	156	139.9	117.1	79.2	115.2	75.4	66.5	161.6	145.5	101.3	149.4	104.1	113.4	66.1	113.9	10.0
118.31	-72.94	354	151	134.9	112.3	75.6	112.0	74.2	61.6	159.9	148.3	105.0	149.3	105.4	118.3	61.3	118.7	10.3
132.04	-70.44	357	147	129.9	107.6	72.4	108.5	72.8	56.7	157.0	150.1	108.3	149.0	106.9	123.2	56.5	123.5	11.2
140.85	-66.63	358	142	125.2	103.3	69.9	104.4	70.7	51.7	153.1	150.5	110.9	148.7	109.0	128.2	51.5	128.5	10.3
147.53	-62.51	359	137	120.3	98.8	67.4	100.3	68.9	46.7	148.8	150.2	113.5	147.5	110.9	133.2	46.5	133.5	7.4
151.18	-57.97	358	132	115.5	94.5	65.5	96.0	66.9	41.7	144.3	148.8	115.6	146.2	113.0	138.2	41.5	138.5	5.8
153.363	-53.091	360	127	111.2	90.8	64.7	91.2	64.0	37.0	139.4	145.9	116.5	145.2	115.9	142.9	36.7	143.3	3.7
153.933	-48.239	359	122	106.7	87.1	64.0	86.6	61.6	32.2	134.5	142.8	117.4	143.5	118.4	147.7	31.8	148.2	1.8
155.331	-43.208	358	116	102.5	83.7	64.1	81.7	58.6	27.7	129.5	138.9	117.4	141.9	121.4	152.1	27.1	152.9	2.0
151.172	-7.256	342	84	75.4	66.7	76.2	45.6	39.5	21.9	93.6	105.2	105.6	124.1	141.1	157.9	18.7	161.3	4.8
75.	-73.	348.	163.	147.	124.	84.	120.	78.	74.	162.	141.	96.	148.	102.	106.	73.4	106.6	N/A (GBM)

Note. The first 10 are on the southern lobe, which contains 94% of the probability. The positions are 5° apart. Positions are given in equatorial (R.A. and decl.) and spacecraft (ϕ , θ) frames. The Large Area Telescope (LAT) boresight is at spacecraft Zenith, $\theta = 0^\circ$. Angles to each detector normal are listed for each position. The final column shows the % probability of the LIGO Sky Map contained in a slice of the arc centered on each position. The 11th position is on the northern lobe, which contains 6% of the probability of the localization of GW150914. The positions behind the Earth to *Fermi* contain 25% of the probability and are not listed here. The final position listed in the table is the best localization for GW150914-GBM. All angles are given in degrees.

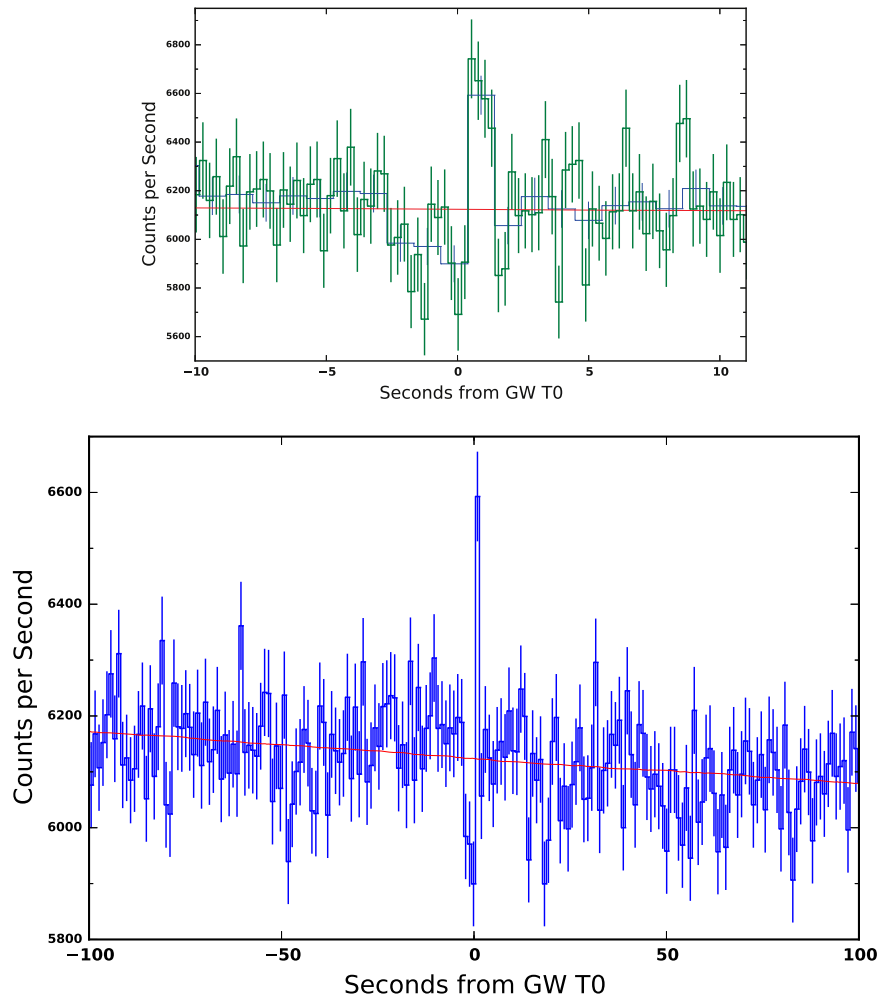


Figure 7. Count rates detected as a function of time relative to the detection time of GW150914, summed over all 14 GBM detectors. NaI data are summed over 50–980 keV and BGO data over 420 keV–4.7 MeV. Time bins are 1.024 s wide, with the same time binning as in Figure 6, and the red line indicates the background level. The blue light curve was constructed from CTTE data, rebinned to optimize the signal-to-noise ratio. The signal-to-noise ratio for this light curve, summed over all detectors in the selected energy range, is 6σ . In the top panel, the 0.256 s CTIME binning is overplotted on the 1.024 s light curve. The dip before the spike associated with GW150914-GBM is not significant. Such dips are common in stretches of GBM data, as can be seen in the longer stretch of data on the bottom panel. A 1600 s stretch of data centered on GW150914-GBM, with 1.024 s binning, shows 100 runs each of positive and negative dips lasting 3 s or longer relative to a third-order polynomial fit background over the 1600 s time interval, with 55 (38) negative (positive) excursions lasting 4 s or longer.

during the optimization of the search procedure, and was the most significant timescale over which GW150914-GBM was detected. We subsequently optimized the phasing of the 1.024 s bins to produce the largest significance, which is higher than the significance in the initial 60 s search window (Figure 2). The shaded region shows this optimized 1.024 s interval, which begins 0.384 s after the GW event, at 09:30:45.775 UT.

The three low 1.024 s bins in Figure 7 that precede the high bin are consistent with a normal background fluctuation. Other similar excursions, positive and negative, are seen in the panel showing the longer time span. The decrease cannot be caused by anything blocking photons: for this energy range, only a very bright and hard transient would be strong enough for a single source going behind the Earth to cause a rate decrease. Nor could a data issue have caused the photons to “move” from the low bins to the high bin that we attribute to GW150914-GBM, because the GBM hardware time-tags individual photons as they arrive. There is a known GBM hardware

anomaly in which dips and peaks in a time history are digitally created. For one second the GBM clock is mis-set by 0.1 s. This has the effect of shifting a block of counts by 0.1 s, leaving a 0.1 s interval with no counts and another 0.1 s interval with double counts—shifted and correct. These “timing glitches” are understood and have been extensively studied since they are readily found by the TGF (Briggs et al. 2013) and GRB offline searches. While there are some variations on this pattern, all timing glitches are definitively revealed by a time interval of duration tens of milliseconds with no counts from any detector. We have examined the data at higher resolution than shown in Figure 7 and no timing glitches are present. We have also investigated the possibility of any telemetry issues or anomalies suggestive of data problems and we find that everything on the spacecraft and in our ground processing was operating nominally.

The lack of a prominent, bright signal in a detector or pair of detectors accounts for the non-detection of this event on board

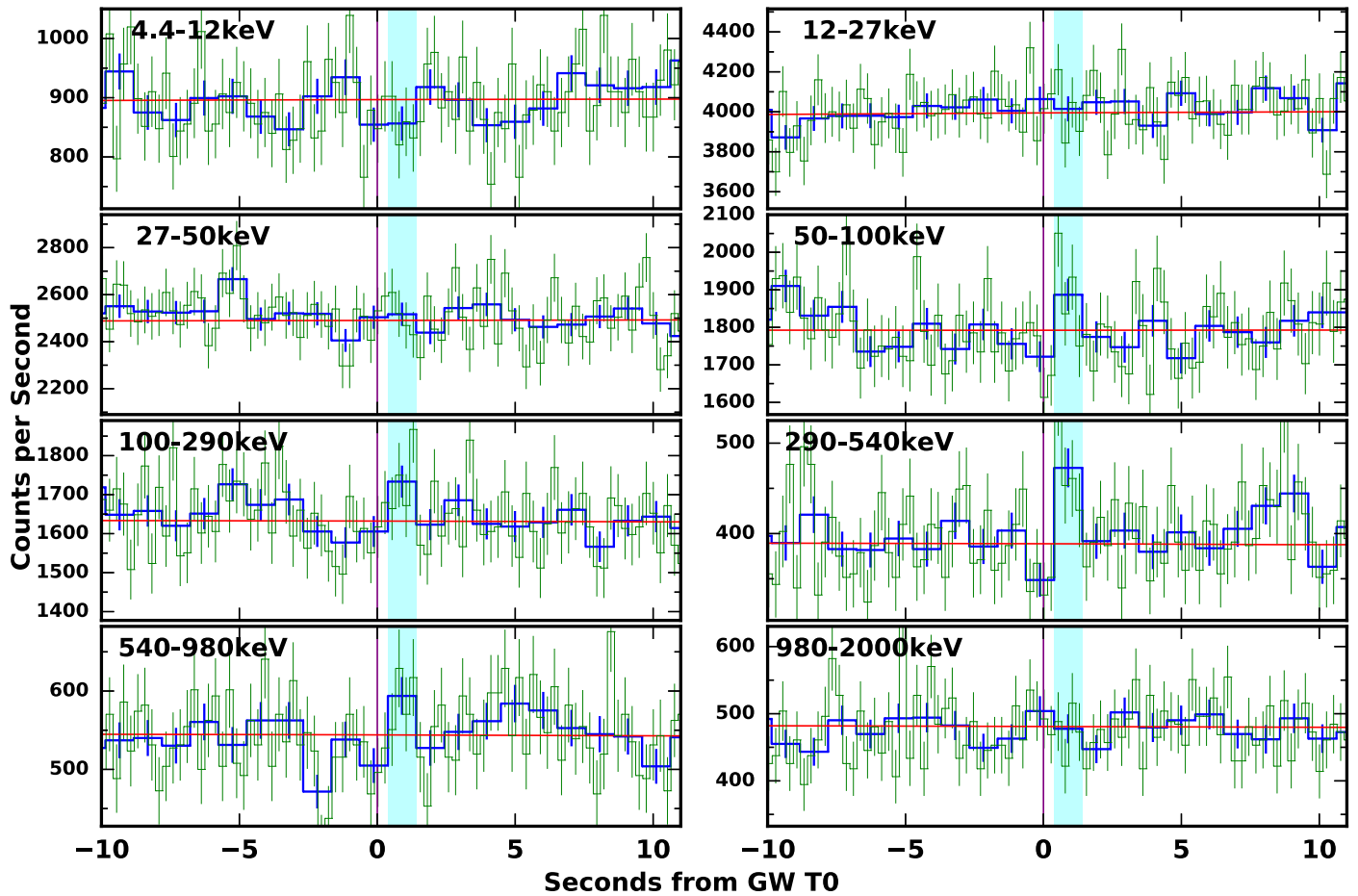


Figure 8. Detected count rates summed over NaI detectors in eight energy channels, as a function of time relative to the start of GW150914. Shading highlights the interval containing GW150914-GBM. Time bins are 1.024 s in duration, with the 0.256 s CTIME light curve overplotted in green and the red line indicating the background level.

and in the undirected offline search. None of the detectors reaches the single-detector threshold of the offline search, indicating an event much weaker than the limiting sensitivity of the undirected search. The fact that all the NaI detectors, and both BGO detectors, register counts above the background fit is unusual. In an *ad hoc* experiment to quantify how unusual it is, we looked through 30 days (1.7 million seconds of livetime) of data for similar features showing high multiplicities of detectors above or below the background level. The signature required both BGOs to exceed background by $\geq 2\sigma$, at least two NaI detectors with $\geq 2\sigma$, and at least six additional NaI detectors with signal levels $\geq 1\sigma$, for a total of eight NaI detectors and two BGO detectors with signal requirements. Three timescales of the 1.024 s binned data: 0.7, 1.0, and 1.4 s, were searched using four search window phases and five energy ranges, including those in the light curve shown in Figure 7.

GW150914-GBM exceeds these requirements (Table 1), with two NaI detectors above 2σ and eight additional NaI detectors above 1σ . The search found 20 candidates (including GW150914-GBM), 14 excesses, and 6 deficits, giving a 90% confidence level upper limit of 27.8 total candidates. If we consider these candidates to be non-astrophysical, this suggests a background rate of one per 6.12×10^4 s implying a chance coincidence of 1.0×10^{-3} for a signal to accidentally match the signature of GW150914-GBM in a 60 s period.

Figures 8 and 9 shows the light curve in the summed NaI and BGO detectors, respectively, divided into the eight native CTIME energy channels, with the energy ranges indicated in the panels. These lightcurves show that GW150914-GBM has a very hard spectrum, with little to no signal below 50 keV and a peak in the spectrum for the NaI detectors in the 290–540 keV band. Above 300 keV, photons deposit little of their energy in the thin NaI detectors so that the measured energy is much lower than the true incident energy. A significant count rate in this energy band in the NaI detectors implies an incident flux of higher-energy photons, consistent with the BGO count spectrum that extends into the MeV energy range. BGO is a higher-Z material and the detectors are thick, so that incident MeV photons deposit most or all of their energy in the scintillator and the measured energy is a good estimate of the incident energy. Both the NaI and the BGO count spectra look reasonable, with no indications that the event is a statistical fluctuation: there are no gaps in the spectra between 50 keV and 980 keV for the NaI detectors and between 420 keV and 4.7 MeV in the BGO detectors, as one would expect if the event were spurious; the signal increases with energy, peaks, and then decreases, as expected from a real source; and the NaI and BGO energy spectra are consistent with each other.

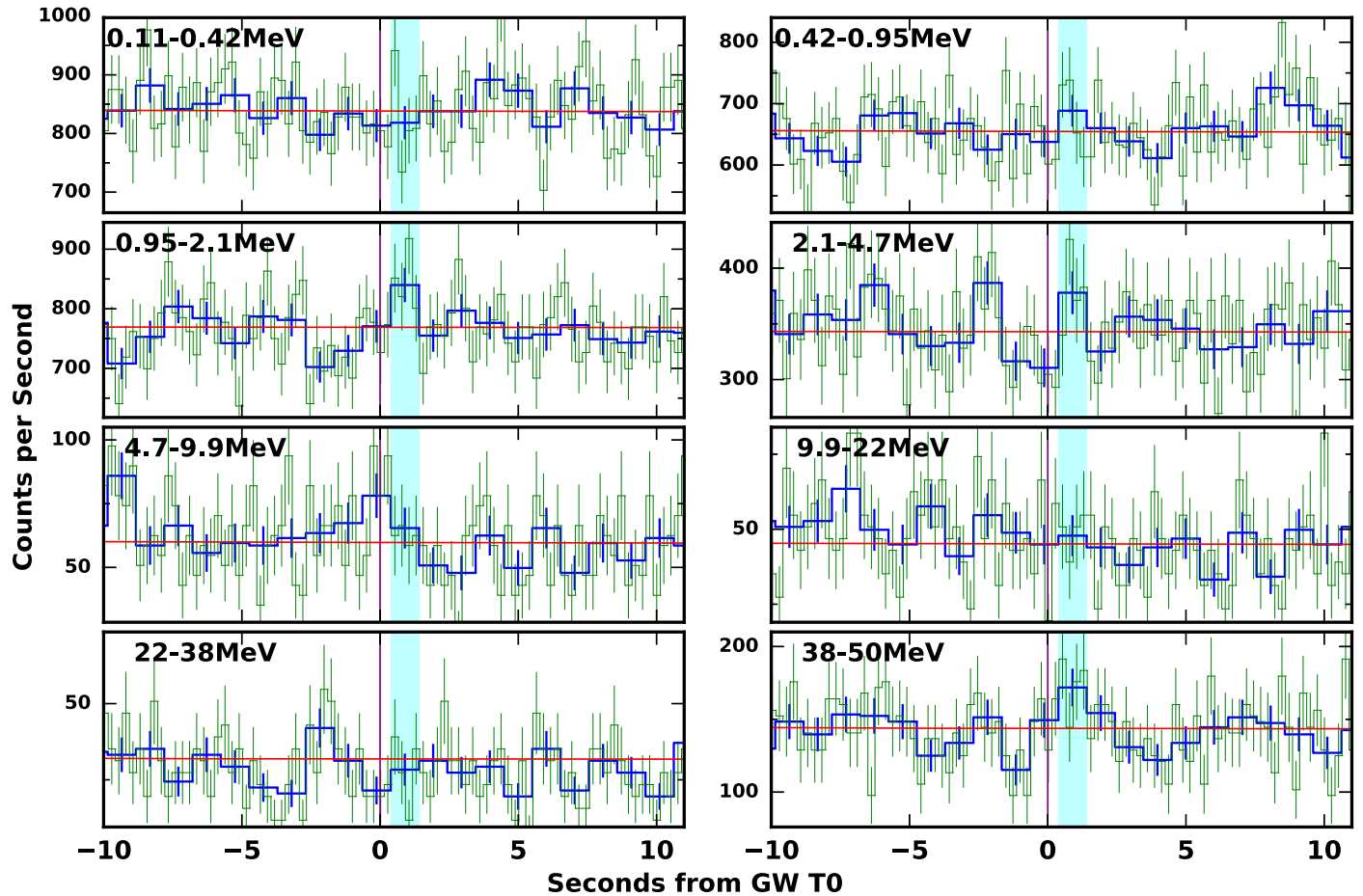


Figure 9. Detected count rates summed over BGO detectors in eight energy channels, as a function of time relative to the start of the GW event. Shading highlights the interval containing GW150914-GBM. Time bins are 1.024 s in duration, with the 0.256 s CTIME light curve overlotted in green and the red line indicating the background level.

APPENDIX D LOCALIZATION OF GW150914-GBM

Source localization involves a comparison of the observed rates in all 12 NaI detectors with the rates expected from a source at 1 of 41,168 positions that cover all of the possible arrival directions in the spacecraft reference frame.

The 50–300 keV energy range is the standard selection for source localization, both to minimize the effect of short timescale variability contributed by galactic sources such as Sco X-1 (which have steeply falling energy spectra above 20 keV) and to maximize the counts in the energy range in which the detector spectral response is very good (response and energy accuracy fall above 300 keV). This energy range captures the peak in the spectral energy distribution for most GRBs. Model rates are calculated for the detector response to sources with the three different energy spectra described in Section 2.1. The most likely arrival direction is the one in which χ^2 is minimized in a comparison of background-subtracted observed and model rates on an all-sky grid of 1° resolution, as described in Connaughton et al. (2015). This process yields a localization in both equatorial and galactic coordinates and a 68% statistical uncertainty radius, σ . The uncertainty region covers all the grid points that lie within 2.3 units of the χ^2 minimum, and σ is calculated assuming the uncertainty region is a circle. In practice, the uncertainty region can be irregular in shape and, for weak events, it may be

composed of disjointed islands, so that σ is a measure of the size of the uncertainty region but is not always a good guide to its shape.

D.1. Standard Localization of GW150914-GBM

The localization of GW150914-GBM finds a best fit to the hard model spectrum and yields a position of R.A., decl. = 57° , -22° with a 68% statistical uncertainty region over 9000 square degrees ($\sigma = 54^\circ$). In addition to the large uncertainty, the χ^2 suggests a bad fit to the observed rates that would have failed a bad- χ^2 cut applied in the regular GBM localization procedure for GRBs (Connaughton et al. 2015). The best-fit location is toward the Earth but the large uncertainty on the location allows an arrival direction from the sky. Figure 6 shows that the rates in the NaI detectors are not very high above background and the differences among them do not allow much discrimination of arrival direction. GBM detectors register signal counts directly from a source and also record a source signal from gamma-rays scattering in the Earth’s atmosphere, with a magnitude determined by the source-Earth-detector geometry. When finding the most likely arrival direction for an event, the localization algorithm fits both a direct and atmospheric component that takes into account the position of the Earth in the spacecraft coordinate system at the time of the observation. At the time GW150914-GBM was detected, only one of the NaI detectors had a favorable Earth-

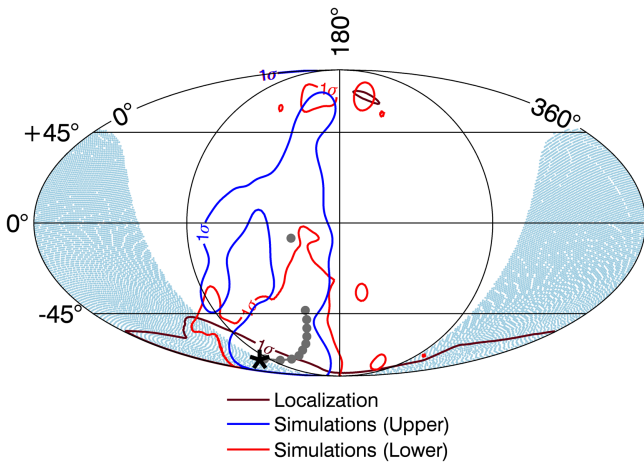


Figure 10. GBM localization of GW150914-GBM using NaI detector counts in the 100–1000 keV energy range, shown in celestial equatorial coordinates. The best localization is marked with an asterisk and the brown contour indicates the 68% confidence level region for this localization. The best GBM localization is just behind the Earth’s limb (shaded blue) with a large uncertainty contour that significantly overlaps the southern lobe of the LIGO location arc (indicated as 11 gray circles). Simulations in the 100–1000 keV range of the localization of a weak source from each of these 11 positions along the LIGO localization arc indicate how well GBM localization is expected to perform for a source as weak as GW150914-GBM with the same source geometry relative to the spacecraft. The red and blue contours show the 68% containment for the simulated locations from the southern (lower) and northern (upper) lobe, respectively. The GBM localization overlaps both sets of simulated localizations, with a better match to those from the southern lobe.

viewing angle. The detector normal of NaI 11 was oriented at 39° to the Earth, yet registered the lowest signal above background of any detector, suggesting that whatever the source direction, the atmospheric component was not large. NaI detectors 0 through 5 were not susceptible to any flux from the atmosphere because they faced the sky with the spacecraft positioned between the detectors and the Earth. There is no weighting in the localization algorithm to disfavor the part of the sky that is occulted by the Earth—the algorithm uses only the relative rates in the NaI detectors to reconstruct the most likely arrival direction after modeling the response to both direct and atmospheric components at each tested sky position (even those behind the Earth), taking into account the position of the Earth when evaluating the atmospheric component.

Since the detection of GW150914, analysis of the LIGO data has resulted in a refinement of the GW event localization, including a new map (The LIGO Scientific Collaboration & Virgo 2015b) that places most of the probability in the southern portion of the original arc, with only 6% in a northern sliver of the arc. Most of the arc lies at a large angle, θ , to the spacecraft zenith, almost entirely under *Fermi*. Figure 1 shows that part of the southern portion of the arc (25% of the probability) is hidden from *Fermi* by the Earth. The rest of the arc lies above the horizon, at low elevation above the Earth to *Fermi*. We note that for sources at low elevation, the atmospheric component of the signal is low relative to the direct component (Pendleton et al. 1999; Harmon et al. 2002), which is compatible with the low count rate observed in NaI 11. The position R.A., decl. = 57° , -22° returned by our localization procedure is roughly consistent with the LIGO arc. Different data interval and background selections of the GBM data used in the localization led in some cases to localizations at the spacecraft

zenith, an indication that the localization process was not converging.

GBM is a background-limited instrument and this event is much weaker than any GRB we would normally localize based on either an on board or offline detection. The signal-to-noise ratio in each detector is low and affected by fluctuations in the background rates. We reported in Blackburn et al. (2015b) that we could not constrain the location of the transient event uncovered in our search. Since then, we have investigated our data more closely.

We do not use the BGO detectors in the standard localization process because their angular response depends only weakly on the source direction compared to the response of the NaI detectors. Also, because the flux from sources detected by GBM declines with increasing energy—and, for GRBs, falls more steeply above $E_{\text{peak}} \sim 100\text{--}500$ keV—source signals are usually more intense in the NaI detectors than in the BGO detectors. For GW150914-GBM, the signals in individual NaI detectors are weak. The fact that there is a detectable signal in the BGO detectors suggests that if the event is real, then for any reasonable source energy spectrum, it arrived from a direction preferentially viewed by BGO detectors relative to NaI detectors. This picture is compatible with a source direction underneath the spacecraft.

We perform simulations to quantify how well we expect to localize weak signals that come from directions along the LIGO arc. We divide the LIGO arc into 11 positions, 10 on the southern portion and 1 in the north, excluding the parts of the arc that were occulted to *Fermi*. The positions are listed in Table 2, which shows each position in celestial equatorial and spacecraft coordinates, the angle to each of the NaI and BGO detectors, and the probability of the LIGO source lying near each position, based on the LIGO location map. The positions are $\sim 5^\circ$ apart, which is comparable to the accuracy with which GBM could localize a weak triggered transient source using the standard localization techniques. NaI 5 is the only NaI detector with a source angle less than 60° for several of the southern lobe positions. Above an incidence angle of 60° , the angular response of the NaI detectors drops significantly. However, the detectors are not shielded, and thus can register counts from any angle, including through the back of the detectors, which can detect gamma-rays or cosmic rays with about 20% efficiency relative to on-axis particles.

We calculate the expected count rates in each detector between 50 and 300 keV using the detector responses for each of the 10 positions along the southern lobe of the LIGO arc and a normalization based on the observed event signal. For each position, we add background rates derived from the observed background rate at the time of the detection of GW150914-GBM, and apply Poisson fluctuations to both source and background in 1000 iterations of the 1 s event at each position. Using the background-subtracted count rates in each simulated event, we assess our ability to localize such a weak source using our standard localization process. The majority of the simulated events are reconstructed near the arc containing the true positions, with large uncertainties. Count rate fluctuations can lead to poor localizations in the wrong part of the sky. We note that a significant number of simulated events (17%) are placed behind the Earth. A simulation of the final position in Table 2 covering the northern lobe of the LIGO arc places 4% of the localizations behind the Earth but, unlike the southern lobe, these localizations behind the Earth have consistently

large σ and bad χ^2 . We conclude that the localization of the observed event GW150914-GBM behind the Earth with a large uncertainty region of 9000 square degrees is not inconsistent with an origin along the LIGO localization arc, most likely on the southern lobe.

D.2. Refined Localization of GW150914-GBM

We attempt to refine the GBM localization by examining a broader energy range than the standard 50–300 keV. Noting from Figure 8 that much of the observed signal occurs above 300 keV, we produced model rates using the soft, medium, and hard spectral models in various energy bands, in the ranges 50–1000, 50–540, 100–1000, and 100–540 keV. We used the standard localization procedure, minimizing χ^2 for the observed rates in each of the energy ranges relative to the model rates in that energy range. The localization in each case returned a similar position for the most likely origin of the source, always slightly behind the Earth, and always at $\theta \sim 160^\circ$. The probability contours are more bounded than those from the 50–300 keV localization. The probability maps cover similar regions of sky for all four localizations. The smallest statistical uncertainty was found using the 100–1000 keV energy band. A minimum was found at R.A., decl. = 75° , -73° with a 68% confidence region covering about 3000 square degrees ($\sigma = 30^\circ$) and a preference for the hard spectral model. The uncertainty contours are broad but constraining. With a source this weak from this direction in the spacecraft frame, we reach the limit of being able to use the angular response of the NaI detectors to localize a source. The measurement of equal rates in most NaI detectors allows the localization to converge to a region under the spacecraft with slight discrimination in favor of one or another detector cluster but no further refinement. We can, however, say that the general source direction is consistent with the LIGO arc and define a fairly large region on the sky from which the signal must originate.

We include only statistical uncertainties in our location map. The standard localization process using the 50–300 keV energy range was found to have a systematic component on the order of 3° – 4° for a sample of 200 triggered GRBs (Connaughton et al. 2015). We do not expect the systematic error to be much different using the 100–1000 keV energy range, particularly when compared to the size of the statistical uncertainty when localizing an event this weak, but we note that our characterization of triggered GRB localizations may not be applicable to these weak events that are more affected by background fluctuations comparable in size to the signal strength. Additionally, although the localization uses the standard GBM procedure, the quality of the localizations has not been assessed using non-standard energy ranges and our uncertainty calculations do not include any systematic component.

Figure 10 shows the best position and the associated 1σ uncertainty contours for the localization performed using data between 100 and 1000 keV. The parts of the LIGO arc visible to *Fermi* are shown as a series of points (with positions listed in Table 2) and the Earth region is shaded. The LIGO arc overlaps the GBM localization in the southern lobe. We also show the 68% containment region of all of the localizations returned by simulations between 100 and 1000 keV of weak sources from positions on the southern and northern lobes. The simulations suggest a broad distribution of possible locations for a given

source position, but we find that the actual localization of GW150914-GBM is quite well constrained to the part of the sky (and Earth) at high θ , consistent with an origin in the southern lobe of the LIGO annulus.

REFERENCES

- Abadie, J., Abbott, B. P., Abbott, R., et al. 2012, *ApJ*, **760**, 12
 Abbott, B. P., Abbott, R., Abbott, T. D., et al. 2016a, *ApJL*, in press (arXiv:1602.08492)
 Abbott, B. P., Abbott, R., Abbott, T. D., et al. 2016b, *PhRvL*, **116**, 061102
 Acernese, F., Agathos, M., Agatsuma, K., et al. 2015, *CQGra*, **32**, 024001
 Band, D., Matteson, J., Ford, L., et al. 1993, *ApJ*, **413**, 281
 Barnes, J., & Kasen, D. 2013, *ApJ*, **775**, 18
 Berger, E. 2014, *ARA&A*, **52**, 43
 Berger, E., Fong, W., & Chornock, R. 2013, *ApJL*, **774**, L23
 Blackburn, L. 2015, Significance of two-parameter coincidence, <https://dcc.ligo.org/LIGOT1500534/public>
 Blackburn, L., Briggs, M. S., Camp, J., et al. 2015a, *ApJS*, **217**, 8
 Blackburn, L., Briggs, M. S., Camp, J., et al. 2015b, *GCN*, 18339
 Briggs, M. S., Connaughton, V., Wilson-Hodge, C., et al. 2011, *GeoRL*, **38**, L02808
 Briggs, M. S., Xiong, S., Connaughton, V., et al. 2013, *JGRA*, **118**, 3805
 Burlon, D., Ghirlanda, G., Ghisellini, G., Greiner, J., & Celotti, A. 2009, *A&A*, **505**, 569
 Collazzi, A. C., Kouveliotou, C., van der Horst, A. J., et al. 2015, *ApJS*, **218**, 11
 Connaughton, V., Briggs, M. S., Goldstein, A., et al. 2015, *ApJS*, **216**, 32
 D’Avanzo, P., Salvaterra, R., Bernardini, M. G., et al. 2014, *MNRAS*, **442**, 2342
 Dwyer, J. R., Grefenstette, B. W., & Smith, D. M. 2008, *GeoRL*, **35**, L02815
 Ellis, J., Mavromatos, N. E., & Nanopoulos, D. V. 2016, arXiv:1602.04764
 Fermi-LAT Collaboration 2016, *ApJL*, **823**, L2
 Ferrigno, C., Savchenko, V., Mereghetti, S., et al. 2015, *GCN*, 18354
 Fong, W., Berger, E., Margutti, R., & Zauderer, B. A. 2015, *ApJ*, **815**, 102
 Giacomazzo, B., Perna, R., Rezzolla, L., Troja, E., & Lazzati, D. 2013, *ApJL*, **762**, L18
 Gruber, D., Goldstein, A., Weller von Ahlefeld, V., et al. 2014, *ApJS*, **211**, 12
 Harmon, B. A., Fishman, G. J., Wilson, C. A., et al. 2002, *ApJS*, **138**, 149
 Hutchins, M. L., Holzworth, R. H., Brundell, J. B., & Rodger, C. J. 2012, *RaSc*, **47**, RS6005
 Jenke, P., Linares, M., Connaughton, V., et al. 2016, *ApJ*, in press
 Kamble, A., & Kaplan, D. L. A. 2013, *IJMPD*, **22**, 1341011
 Kelley, L. Z., Mandel, I., & Ramirez-Ruiz, E. 2013, *PhRvD*, **87**, 123004
 Kochanek, C. S., & Piran, T. 1993, *ApJL*, **417**, L17
 Koshut, T. M., Kouveliotou, C., Paciesas, W. S., et al. 1995, *ApJ*, **452**, 145
 Li, L.-X., & Paczyński, B. 1998, *ApJL*, **507**, L59
 Li, X., Zhang, F.-W., Yuan, Q., et al. 2016, arXiv:1602.04460
 LIGO Scientific Collaboration, Aasi, J., Abbott, B. P., et al. 2015, *CQGra*, **32**, 074001
 Loeb, A. 2016, *ApJL*, **819**, L21
 Lyutikov, M. 2016, arXiv:1602.07352
 Mayer, L., Kazantzidis, S., Madau, P., et al. 2007, *Sci*, **316**, 1874
 Meegan, C., Lichti, G., Bhat, P. N., et al. 2009, *ApJ*, **702**, 791
 Metzger, B. D., Martínez-Pinedo, G., Darbha, S., et al. 2010, *MNRAS*, **406**, 2650
 Morsony, B. J., Workman, J. C., & Ryan, D. M. 2016, *ApJL*, in press (arXiv:1602.05529)
 Pendleton, G. N., Briggs, M. S., Kippen, R. M., et al. 1999, *ApJ*, **512**, 362
 Perna, R., Lazzati, D., & Giacomazzo, B. 2016, *ApJL*, **821**, L18
 Rodger, C. J., Brundell, J. B., Holzworth, R. H., & Lay, E. H. 2009, in Conf. Proc. 1118, Coupling 645 of Thunderstorms and Lightning Discharges to Near-Earth Space, ed. N. B. Crosby, T.-Y. Huang, & M. J. Rycroft (Melville, NY: AIP), 15
 Ross, S. M. 2014, Introduction to Probability Models (New York: Academic)
 Said, R. K., Cohen, M. B., & Inan, U. S. 2013, *JGRD*, **118**, 6905
 Said, R. K., Inan, U. S., & Cummins, K. L. 2010, *JGRD*, **115**, D23108
 Savchenko, V., Ferrigno, C., Mereghetti, S., et al. 2016, *ApJL*, **820**, L36
 Siellez, K., Boër, M., & Gendre, B. 2014, *MNRAS*, **437**, 649
 Tanaka, M., & Hotokezaka, K. 2013, *ApJ*, **775**, 113
 Tanvir, N. R., Levan, A. J., Fruchter, A. S., et al. 2013, *Natur*, **500**, 547
 Tavani, M., Pittori, C., Verrecchia, F., et al. 2016, *ApJL*, **825**, L4
 The LIGO Scientific Collaboration & Virgo 2015a, *GCN*, 18388

The LIGO Scientific Collaboration & Virgo 2015b, GCN, 18858
The LIGO Scientific Collaboration & Virgo 2015c, GCN, 18851
The LIGO Scientific Collaboration & Virgo 2015d, GCN, 18330
Troja, E., Rosswog, S., & Gehrels, N. 2010, [ApJ](#), **723**, 1711
von Kienlin, A., Beckmann, V., Rau, A., et al. 2003, [A&A](#), **411**, L299
von Kienlin, A., Meegan, C. A., Paciesas, W. S., et al. 2014, [ApJS](#), **211**, 13

Wanderman, D., & Piran, T. 2015, [MNRAS](#), **448**, 3026
Wilson-Hodge, C. A., Case, G. L., Cherry, M. L., et al. 2012, [ApJS](#), **201**, 33
Yamazaki, R., Asano, K., & Ohira, Y. 2016, [PTEP](#), **2016**, 051E01
Yang, B., Jin, Z.-P., Li, X., et al. 2015, [NatCo](#), **6**, 7323
Zhang, B. 2016, arXiv:1602.04542